

# Two-Level System Damping in a Single-Crystal Silicon Optomechanical Resonator

B.D. Hauer,\* P.H. Kim, C. Doolin, F. Souris, and J.P. Davis†

*Department of Physics, University of Alberta,*

*Edmonton, Alberta, Canada T6G 2E9*

(Dated: August 1, 2022)

## Abstract

Nanomechanical resonators have recently demonstrated great potential for use as versatile tools in a number of emerging quantum technologies. However, the performance of these systems is restricted by the decoherence of their fragile quantum states, necessitating a thorough understanding of their dissipative coupling to the surrounding environment. In amorphous solids, these dissipation channels are dominated at low temperatures by parasitic coupling to two-level system (TLS) defects within the resonator, however, quantitative verification of this model has never been demonstrated for a crystalline material. Here, we present simultaneous thermal ringdown measurements of four mechanical modes in a cryogenically-cooled, single-crystal silicon optomechanical resonator. Analyzing the low-temperature dependence of the device's mechanical damping rate, we demonstrate for the first time quantitative agreement with the standard model for TLS dissipation in crystalline resonators. We identify the microscopic origin of these TLS, elucidating a route by which they could be removed entirely, or engineered such that the resonator couples to a single intrinsic quantum defect.

---

\* bhauer@ualberta.ca

† jdavis@ualberta.ca

Over the past decade, quantum behaviour has been observed in a number of nanomechanical resonators, including motional ground state cooling [1–3], preparation into squeezed states [4, 5], and nonclassical interaction with electromagnetic fields [6–8]. This level of quantum control has generated significant interest for the use of nanoresonators in quantum applications, such as coherent interfacing between two nonclassical degrees of freedom [9–11], storage of quantum information [1, 7, 8], and quantum-limited force/torque sensing [12, 13]. However, it is crucial that the nanomechanical resonator maintain its quantum coherence for the duration of the intended operation. For instance, to perform quantum state transfer between the optical and mechanical degrees of freedom of an optomechanical resonator – a prerequisite for numerous mechanically-mediated quantum information protocols [6–9, 14–17] – the phononic and photonic modes of the device must couple faster than the rate at which the phononic state decoheres [18]. For a mechanical resonator with angular frequency,  $\omega_m$ , coupled at its damping rate,  $\Gamma$ , to an environmental bath, this rate is given by  $\Gamma_{\text{th}} = n_{\text{th}}\Gamma$ , where  $n_{\text{th}} = (e^{\hbar\omega_m/k_B T} - 1)^{-1}$  is the bath’s thermal phonon occupation at temperature  $T$  [18]. Therefore, in order to minimize decoherence in nanomechanical resonators, such that they can be used as a viable quantum resource, it is critical to focus on reducing their damping at low temperatures.

Though dissipation in mechanical systems can arise from a number of sources, energy loss is often caused by coupling between motion of the resonator and its intrinsic material defects [19]. In the simplest treatment, these defects can be modelled as two-level systems (TLS) with an energy separation of  $E = \sqrt{\Delta^2 + \Delta_0^2}$ , realized by tunneling with a characteristic energy,  $\Delta_0$ , between the two lowest-energy configurational states of the defect, which are split by an asymmetry energy,  $\Delta$  [20]. For a non-resonant interaction at low frequencies ( $\hbar\omega_m < E$ ), local strain variations due to the motion of the resonator distort the environment of the TLS defects, perturbing their energy separation and causing them to interact with surrounding phonons to relax back to thermal equilibrium. This leads to a TLS-induced mechanical damping rate [20]

$$\Gamma_{\text{TLS}} = \frac{\gamma^2}{\rho c^2 k_B T} \int_0^\infty \int_0^\infty \left(\frac{\Delta}{E}\right)^2 \text{sech}^2\left(\frac{E}{2k_B T}\right) \tau^{-1}(\Delta, \Delta_0) h(\Delta, \Delta_0) d\Delta d\Delta_0, \quad (1)$$

where  $\gamma$ ,  $\rho$ , and  $c$  are the deformation potential, density, and speed of sound of the resonator’s material, with  $\tau^{-1}(\Delta, \Delta_0)$  being the rate at which the perturbed TLS ensemble relaxes back to equilibrium (see Supplementary Information).

The function  $h(\Delta, \Delta_0)$  in Eq. (1) describes the distribution of the tunneling and asymmetry

energies of the TLS defects due to their varying environments, and has a profound effect on the temperature dependence of the mechanical damping rate. Acoustic dissipation due to TLS defects has been thoroughly studied in amorphous solids, where lack of long range order causes a broad distribution in these energies, corresponding to the energy distribution function  $h(\Delta, \Delta_0) \propto 1/\Delta_0$ . This results in a damping rate that varies as  $\Gamma \sim T^3$  at low temperatures, experimentally verified by numerous cryogenic measurements of glassy materials [21]. An extension to this model to include crystalline materials was proposed by Phillips [22], whereby defects in an otherwise ordered lattice are treated by introducing a well-defined tunneling energy,  $\bar{\Delta}_0$ , with a Gaussian distribution in the asymmetry energy, centered around  $\Delta = 0$  with a width  $\delta\Delta$ . Mathematically, this energy distribution function is expressed as

$$h(\Delta, \Delta_0) = D_0 \sqrt{\frac{2}{\pi}} \frac{1}{\delta\Delta} e^{-\frac{1}{2} \left(\frac{\Delta}{\delta\Delta}\right)^2} \delta(\Delta_0 - \bar{\Delta}_0), \quad (2)$$

where  $D_0$  is the average spatial density of the TLS defects and  $\delta(\Delta_0 - \bar{\Delta}_0)$  is a Dirac delta function centered on  $\bar{\Delta}_0$ . Using this TLS energy distribution to calculate the mechanical damping rate given by Eq. (1), a drastically different low-temperature dependence of  $\Gamma \sim T$  is expected [22]. However, with the exception of qualitative agreement with this model in early work on single-crystal silicon torsional oscillators [23, 24], recent measurements of resonators fabricated from crystalline materials, including silicon [25], gallium arsenide [26], ultrananocrystalline diamond [27], carbon nanotubes [28] and quartz [29], have demonstrated a considerably weaker  $\Gamma \sim T^{1/3}$  dependence at low temperatures. This observed sublinear temperature dependence has been rationalized as occurring due to the large strain that results from the external drive fields applied to these resonators [30], or possibly their beamlike geometries [31, 32]. Regardless, until now quantitative agreement with the Phillips model has never been observed.

Here, we present measurements of the damping rate in a thermally-driven, single-crystal silicon nanomechanical resonator using a simplified version of the optomechanically-mediated ringdown technique developed by Meenehan *et al.* [33]. Using our approach, which circumvents the need for single photon detectors and the requirement that the device must exist in the sideband-resolved regime, we determine the mechanical damping rate of the device over three orders of magnitude in temperature from 10 mK to 10 K. Fitting these data, we demonstrate for the first time quantitative agreement with the standard tunneling model for damping due to TLS defects embedded in a crystalline material for four of the resonator's mechanical modes. Furthermore, we show that the

dissipation in each mode is ultimately limited by temperature-independent radiation of acoustic energy into the bulk substrate [34, 35]. From this analysis, we extract information about the energy distribution and density of the TLS ensembles that couple to the motion of the device, and conclude that they are caused by p-type dopants within the silicon for mechanical modes with a widely distributed spatial strain profile, while modes with more localized strains couple to defects at the surfaces of the resonator. By identifying the TLS defects in this manner, it should be possible to remove them completely, reducing both damping and decoherence in future generations of devices.

## I. CRYOGENIC OPTOMECHANICAL RINGDOWN MEASUREMENTS

The optomechanical device measured in this paper (see Fig. 1c,d) consists of a half-ring mechanical resonator partially surrounding a whispering gallery mode microdisk cavity, both of which are fabricated from single-crystal silicon. The device is mounted to the mixing chamber plate of a dilution refrigerator and measured using a gated homodyne detection scheme (Fig. 1a – see Methods and Supplementary Information for details), capable of simultaneously transducing the motion of several mechanical modes of the half-ring resonator (Fig. 1f-i) with sub-microsecond resolution in the time domain.

Due to the large disparity between the energies of the optical mode (hundreds of THz) and the mechanical modes (tens of MHz), coupled with the rapidly diminishing thermal conductivity of silicon at low temperatures [36], even small input powers to the optical cavity act to massively heat the mechanics. This heating is modelled as a mechanical mode simultaneously coupled at its intrinsic damping rate,  $\Gamma_i$ , to the thermal environment of the fridge, and at a rate,  $\Gamma_p$ , to a hot phonon bath generated by absorption of cavity photons, with the total damping rate of the system given by  $\Gamma = \Gamma_i + \Gamma_p$ . If light is coupled into the optical cavity at time  $t = t_0$ , the average phonon occupancy of the mechanical mode as a function of time is then given by [33]

$$\langle n \rangle (t) = \langle n \rangle (t_0) e^{-\Gamma(t-t_0)} + n_{\text{eq}} (1 - e^{-\Gamma(t-t_0)}). \quad (3)$$

Here,  $n_{\text{eq}} = (n_{\text{th}}\Gamma_i + n_p\Gamma_p) / \Gamma$  is the equilibrium phonon occupation of the mode, with  $n_{\text{th}}$  and  $n_p$  being the average phonon occupancies of the environmental and photon-induced baths, respectively (see Supplementary Information). We note that for the temperatures considered here,

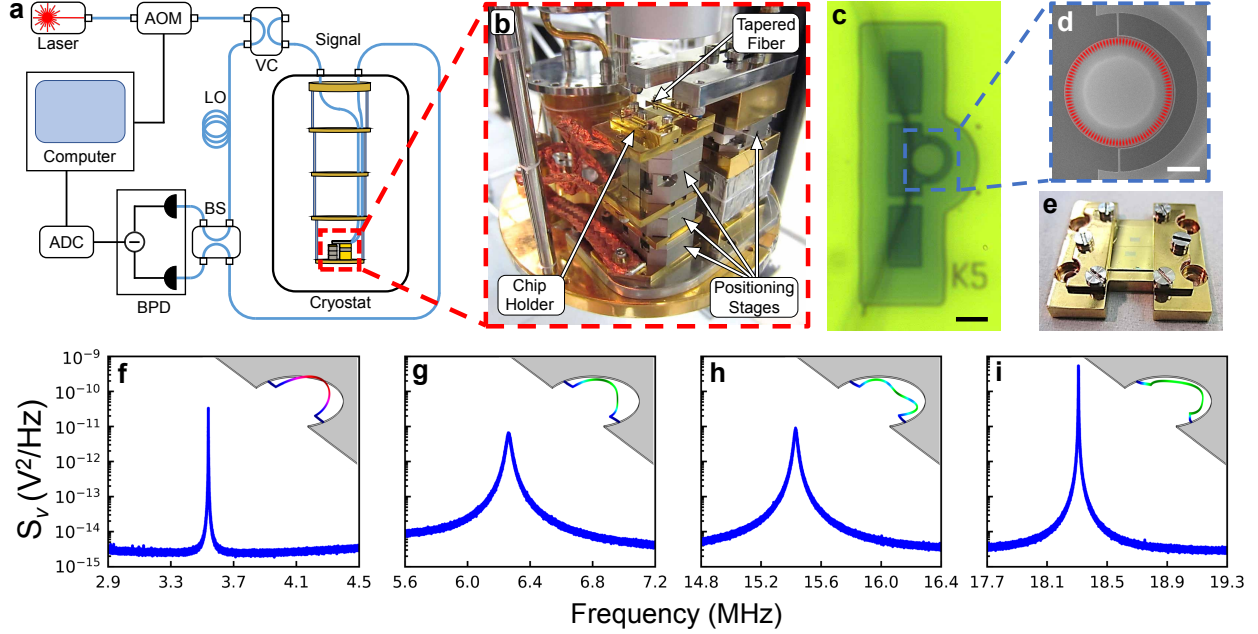


**FIG. 1. Optomechanical coupling apparatus and device.** **a**, Simplified schematic of the gated homodyne optomechanical detection system (see Supplementary Information for details). (AOM = acousto-optic modulator, VC = variable coupler, LO = local oscillator, BS = beam splitter, BPD = balanced photodetector, ADC = analog-to-digital converter). **b**, Low-temperature coupling apparatus on the mixing chamber plate of the dilution refrigerator, capable of reaching a base temperature of 10 mK [37]. **c**, Optical microscope image and **d**, zoomed-in scanning electron micrograph of the optomechanical device studied in this work: a mechanical half-ring resonator coupled to a 10  $\mu\text{m}$  diameter optical microdisk. Overlaid in red is a finite element method (FEM) simulation showing the magnitude of the electric field for the optical whispering gallery mode used in this work. Scale bars are **c**, 10  $\mu\text{m}$  and **d**, 3  $\mu\text{m}$ . **e**, Image of the chip in its gold-plated holder, highlighting the 210 nm thick gold layer added to the silicon to increase the thermalization of our devices. **f-i**, The voltage spectral density,  $S_v$ , obtained by continuously monitoring the resonator’s mechanical motion in exchange gas at 4.2 K. Measurements were performed with 10  $\mu\text{W}$  of optical power input to the fridge (input power of  $P_{\text{in}} = 7.5 \mu\text{W}$  at the microdisk) and 2.6 mW in the LO. Inset are FEM simulations of the displacement profiles for **f**, the fundamental out-of-plane torsional mode (3.53 MHz), along with the **g**, “side-to-side” (6.28 MHz), **h**, antisymmetric “breathing-like” (15.44 MHz), and **i**, symmetric “breathing-like” (18.31 MHz) in-plane flexural modes. Red (green) indicates out-of-plane (in-plane) motion, while blue denotes zero displacement.

$$n_p \gg n_{\text{th}} \text{ and } \Gamma \approx \Gamma_p, \text{ such that } n_{\text{eq}} \approx n_p.$$

This rapid heating (see Fig. 2) prevents one from continuously monitoring the device’s motion at low temperatures. However, by performing time-resolved measurements of the mechanical resonator (see Methods) and looking at its phonon occupancy for  $t < 1 \mu\text{s}$ , we show that the device is initially thermalized to the fridge, as seen in Fig. 2a. Furthermore, we capitalize on this

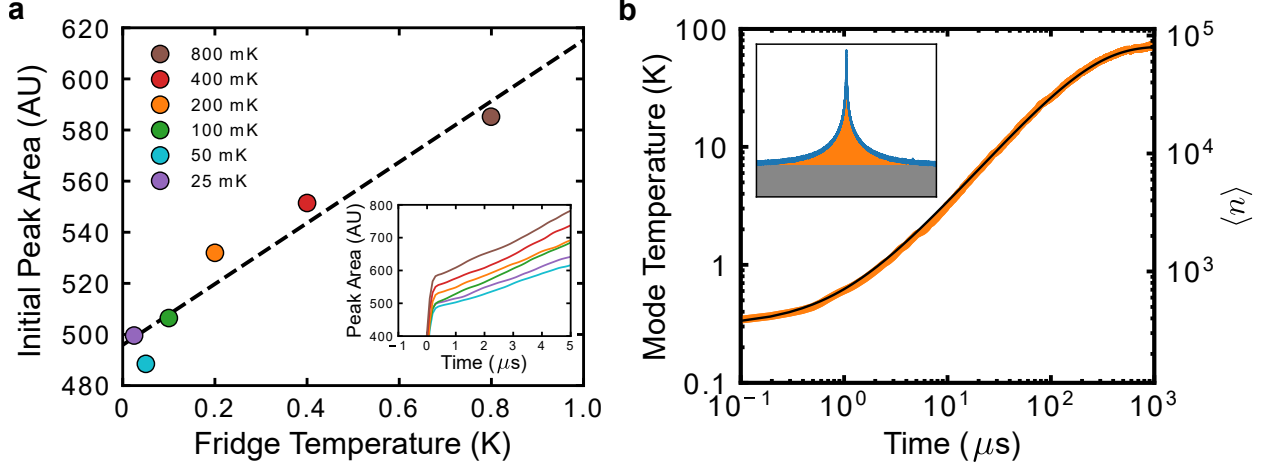


**FIG. 2. Single pulse measurements and mode temperature calibration.** **a**, Area under the peak in the voltage spectral density (including contributions from both the mechanical signal and imprecision noise) at the beginning of the measurement pulse for the 18.31 MHz mode plotted versus fridge temperature. For high input powers ( $P_{\text{in}} = 75 \mu\text{W}$ ), the shot-noise of the optomechanical measurement is sufficiently suppressed to resolve the mode's initial phonon occupation. Fitting this linear trend (dashed line), we calibrate the peak area in terms of the mechanical mode temperature (see Supplementary Information). Inset highlights the rapid increase in the peak area during the first  $5 \mu\text{s}$  of the measurement for each temperature (colour-coded to match the main figure), taken by averaging data from 5000 individual optical pulses of 4 ms in length. **b**, A typical heating curve corresponding to the point in **a** with the fridge temperature at 200 mK. The data (orange) is calibrated in terms of both temperature and average phonon occupancy, showing that the mechanical mode heats to  $T \approx 80 \text{ K}$  within the first millisecond. The solid black line is a fit to Eq. (3), used to extract the initial and final phonon occupancy of the mode, along with its total damping rate,  $\Gamma$ . Inset shows the voltage spectral density of the mechanical resonance over the  $\sim 1.2 \text{ MHz}$  bandwidth window used for these measurements (see Methods). The orange illustrates the area under the peak due to mechanical motion, while grey indicates the noise floor.

optically-induced heating to implement a pump/probe measurement technique [33], as illustrated in the inset of Fig. 3a. This allows one to observe the thermalization of the laser-heated mechanical mode back to the fridge temperature at its intrinsic damping rate according to

$$\frac{\langle n \rangle_i}{\langle n \rangle_f} = \frac{(n_{\text{eq}} - n_{\text{th}}) e^{-\Gamma_i t_{\text{off}}} + n_{\text{th}} + n_{\text{imp}}}{n_{\text{eq}} + n_{\text{imp}}}. \quad (4)$$

Here,  $\langle n \rangle_i$  and  $\langle n \rangle_f$  are the measured phonon occupancies of the mechanical mode (including the apparent contribution,  $n_{\text{imp}}$ , due to imprecision noise) at the beginning of the probe pulse and at the end of the pump pulse, while  $t_{\text{off}}$  is the time delay between turning off the pump pulse and turning on the probe pulse (see Supplementary Information). Note that in Eq. (4), as well as the

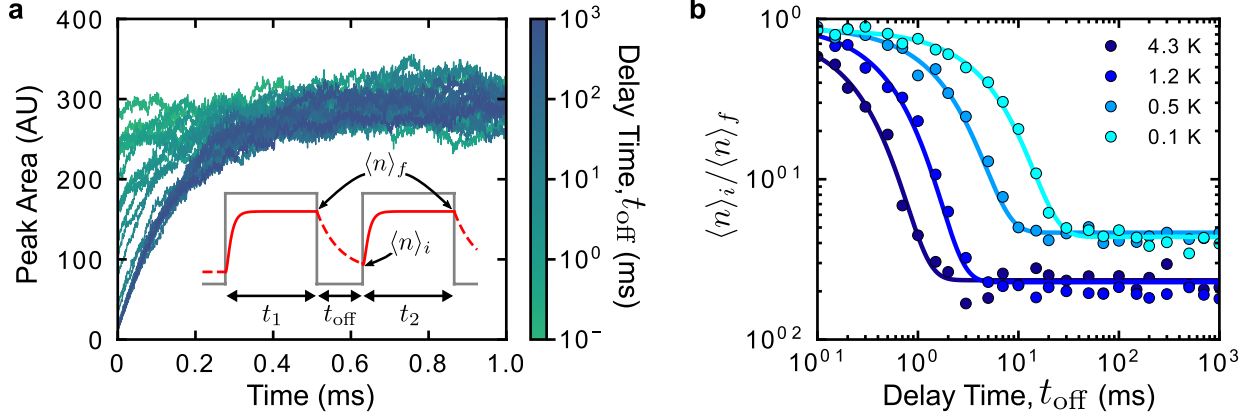


FIG. 3. **Optomechanical thermal ring-up and ring-down measurements.** **a**, The first millisecond of pulsed data for the 18.31 MHz mechanical mode at the fridge base temperature of 10 mK obtained by averaging 500 individual probe pulses, each 2 milliseconds in length. Measurements are performed with varying delay times between the pump and probe pulses (both with  $P_{\text{in}} = 7.5 \mu\text{W}$ ) as indicated by the colour bar. These traces are fit with Eq. (3) to extract their initial and final occupations. Inset is a schematic of the pump-probe sequence. The grey line indicates the state of the laser (high = on, low = off), with the solid (dashed) red line being the average occupancy of the mechanical mode with the laser on (off). **b**, Thermally excited ringdown measurements at a number of fridge temperatures. The solid lines are fits to the data using Eq. (4), allowing extraction of the intrinsic damping rate at each temperature. The disparity in the noise floor between the low temperature (0.1 K, 0.5 K) and high temperature (1.2 K, 4.3 K) data results from varying levels of optomechanical transduction (*i.e.* small variations in input power, optical coupling to the device, etc.) between data runs, and does not have an effect on the extracted intrinsic mechanical damping rate.

experiment, we have chosen the lengths of the pump pulse,  $t_1$ , and probe pulse,  $t_2$ , to be equal, as well as satisfy  $t_1 = t_2 \gg \Gamma^{-1}$  such that  $\langle n \rangle_f = n_{\text{eq}} + n_{\text{imp}}$  at the end of both pulses. By varying the delay between pulses and fitting the data to Eq. (4), as seen in Fig. 3b, we can extract the intrinsic mechanical damping rate of the device, allowing us to map out its low-temperature dependence.

## II. RESULTS

### A. Quantitative Agreement with the Standard Tunneling Model

Measurements of the damping rate for each of the four studied mechanical modes were performed with temperatures varying from 10 mK to 10 K. While each mode exhibits qualitatively

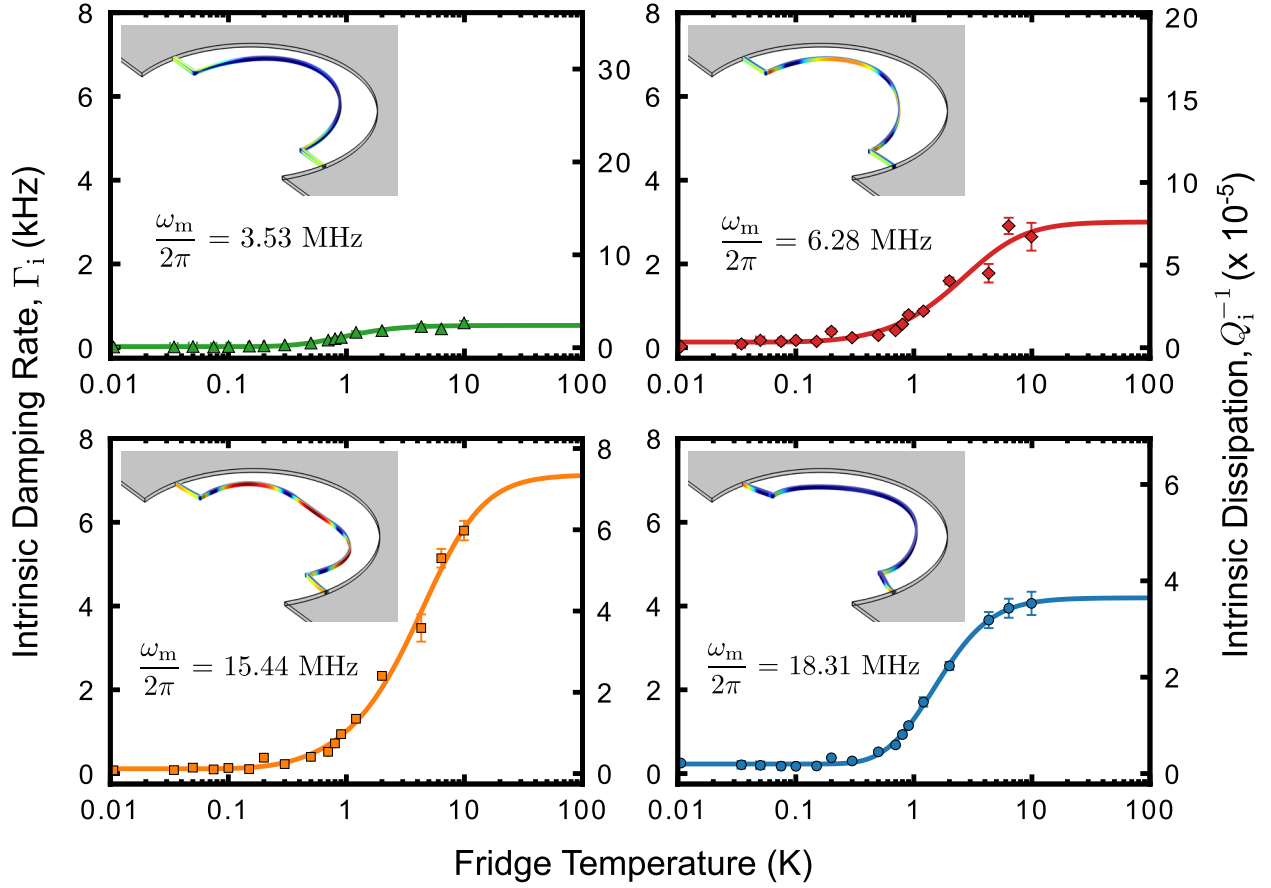


FIG. 4. **Intrinsic damping rate versus temperature.** The intrinsic damping rate,  $\Gamma_i$ , measured for each of the four studied mechanical modes plotted versus temperature, with the right axis displaying their intrinsic dissipation,  $Q_i^{-1} = \Gamma_i/\omega_m$ . Markers in each plot represent the experimentally-determined damping rate extracted from fits of Eq. (4) to data similar to that seen in Fig. 3b, with error bars representing a single standard deviation in the uncertainty of the fit. Solid line fits show excellent agreement between the data and Eq. (5), demonstrating the temperature dependence of the mechanical damping rate according to the Phillips model, as well as the low-temperature plateau due to phonon radiation. Inset are the logarithm of the normalized strain energy density for each of the mechanical modes, highlighting the fact that the 3.53 MHz and 18.31 MHz modes have smaller spatial strain profiles than the 6.28 MHz and 15.44 MHz modes, as characterized by their effective strain volumes (see Supplementary Information). The parameters extracted from these fits are summarized in Tables I and II.

similar behaviour, as seen in Fig. 4, quantitative analysis is performed by fitting the data to

$$\Gamma_i(T) = \Gamma_{\text{TLS}}(T) + \Gamma_0, \quad (5)$$

$\omega_m/2\pi$ (MHz)	$V_{\text{str}}$ ( $\mu\text{m}^3$ )	$\bar{\Delta}_0$ ( $\mu\text{eV}$ )	$\delta\Delta$ ( $\mu\text{eV}$ )	$D_0$ ( $\text{m}^{-3}$ )	$N$
3.53	316	$60 \pm 34$	$228 \pm 64$	$1.3 \times 10^{20}$	4.2
6.28	524	$18 \pm 36$	$754 \pm 178$	$3.2 \times 10^{21}$	168
15.44	870	$55 \pm 21$	$780 \pm 99$	$6.1 \times 10^{21}$	527
18.31	207	$192 \pm 45$	$161 \pm 66$	$4.3 \times 10^{20}$	8.8

TABLE I. Summary of the tunneling energy,  $\bar{\Delta}_0$ , and spread in asymmetry energies,  $\delta\Delta$ , as well as defect density,  $D_0$ , and number,  $N$ , for the TLS ensembles contained within the effective strain volume,  $V_{\text{str}}$ , of each mechanical mode. The energy parameters are directly extracted from fits of Eq. (5) to the data in Fig. 4, while the TLS defect density and number are inferred using the material values for silicon found in the literature (see Supplementary Information). The uncertainties in  $\bar{\Delta}_0$  and  $\delta\Delta$  are their standard deviations from the fit. The effective strain volumes are found from FEM simulations of the strain energy density for each mechanical mode (see Supplementary Information). Here it can be seen that the two mechanical modes with large effective strain volumes (6.28 MHz, 15.44 MHz) couple to a greater number of TLS defects, exhibiting a wider spread in their asymmetry energies as compared to the two modes with smaller effective strain volumes (3.53 MHz, 18.31 MHz).

where  $\Gamma_{\text{TLS}}$  is the temperature-dependent TLS damping rate according to the Phillips model found by numerically integrating Eq. (1), while  $\Gamma_0$  is the temperature-independent damping rate due to acoustic radiation that dominates at low temperatures. Excellent agreement with the Phillips model is demonstrated for each of the four mechanical modes studied here, with the extracted parameters summarized in Tables I and II.

We remark that due to the anisotropic nature of silicon’s crystalline structure, each mechanical mode couples to a slightly different ensemble of TLS, with varying values of  $\bar{\Delta}_0$  and  $\delta\Delta$ , as seen in Table I. Notably, mechanical modes with a larger spatial extent to their strain profiles (6.28 MHz, 15.44 MHz – see Fig. 4), as quantified by their effective strain volume,  $V_{\text{str}}$  (see Supplementary Information), exhibit a larger spread in the asymmetry energy distribution,  $\delta\Delta$ , compared to the modes with more localized strain profiles (3.53 MHz, 18.31 MHz). Mechanical modes with a larger  $V_{\text{str}}$  thus sample a broader distribution of TLS.

## B. Two-Level System Defect Density

Using the material properties of boron-doped silicon from the literature ( $\rho = 2330 \text{ kg/m}^3$  [25],  $c = 5870 \text{ m/s}$  [38] and  $\gamma = 3 \text{ eV}$  [38, 39]), we determine the TLS spatial density,  $D_0$ , and calculate the total number of TLS defects sampled by each mechanical mode as  $N = D_0 V_{\text{str}}$  (see Sup-

$\omega_m/2\pi$ (MHz)	$Q_0$ $\times 10^5$	$\Gamma_0/2\pi$ (Hz)	$\Gamma_{\text{th}}/2\pi$ (Hz)	$\tau_{\text{th}}$ ( $\mu\text{s}$ )	$\tilde{\Gamma}_{\text{TLS}}/2\pi$ (kHz)	$\Gamma_p/2\pi$ (kHz)	$\Gamma_{\text{HT}}/2\pi$ (kHz)
3.53	$7.7 \pm 3.3$	$4.6 \pm 1.9$	$283 \pm 119$	$562 \pm 236$	0.09	$0.722 \pm 0.056$	$0.710 \pm 0.004$
6.28	$2.9 \pm 1.8$	$22 \pm 13$	$756 \pm 464$	$211 \pm 129$	0.48	$15.9 \pm 0.87$	$32.34 \pm 0.04$
15.44	$7.5 \pm 3.2$	$20.5 \pm 8.9$	$284 \pm 123$	$561 \pm 242$	1.14	$12.2 \pm 0.64$	$23.29 \pm 0.02$
18.31	$4.6 \pm 0.6$	$39.7 \pm 5.6$	$460 \pm 64$	$346 \pm 48$	0.67	$0.879 \pm 0.027$	$1.521 \pm 0.006$

TABLE II. Quality factor,  $Q_0$ , damping rate,  $\Gamma_0$ , decoherence rate,  $\Gamma_{\text{th}}$ , and decoherence time,  $\tau_{\text{th}}$ , at low temperatures ( $T < 100$  mK) where the dissipation is dominated by the radiation of phononic energy from each mechanical mode. Also included are the high temperature ( $T \gtrsim 10$  K) intrinsic damping rates due to TLS defects,  $\tilde{\Gamma}_{\text{TLS}}$ , and the hot phonon bath,  $\Gamma_p$ , as well as the high temperature value,  $\Gamma_{\text{HT}}$ , observed with continuous measurement.  $\Gamma_0$  ( $\tilde{\Gamma}_{\text{TLS}}$ ) is inferred from the low (high) temperature limit of the fits to the data in Fig. 4, with  $Q_0$ ,  $\Gamma_{\text{th}}$ , and  $\tau_{\text{th}}$  calculated from  $\Gamma_0$  using the lowest measured temperature of 10 mK.  $\Gamma_p$  is found by averaging over values extracted from low temperature ( $T \leq 500$  mK) fits of Eq. (3) to the data in Fig. 3a (as well as similar data for the other three mechanical modes), with the uncertainty given as their standard deviation.  $\Gamma_{\text{HT}}$  is found by fitting the spectra in Fig. 1f-i to the appropriate power spectral density function [40]. The uncertainty for all values (except  $\Gamma_p$ ) is given as the standard deviation from their fits, using standard error propagation where necessary. By comparing the sum of  $\tilde{\Gamma}_{\text{TLS}}$  and  $\Gamma_p$  to  $\Gamma_{\text{HT}}$ , we see that coupling to TLS defects limits the intrinsic damping rate at high temperatures for the torsional mode (3.53 MHz) and the symmetric breathing-like mode (18.31 MHz), both of which exhibit relatively smaller effective strain volumes (see Table I). However, this is not the case for the other two mechanical modes with large strain distributions, implying that another internal dissipation mechanism, such as thermoelastic damping [41], dominates at high temperature.

plementary Information). These results are highlighted in Table I, showing that we mechanically couple to TLS ensembles with densities ranging from  $10^{20} - 10^{22} \text{ m}^{-3}$ , corresponding to as few as four defects. We note, however, that the  $\gamma^{-4}$  dependence in  $D_0$  means that small variations in  $\gamma$ , for which a range of values are reported in the literature ( $\gamma \sim 2 - 5$  eV [38, 39]), can lead to large differences in the calculated TLS densities, and consequently, number of sampled defects. Furthermore, we have neglected to account for the true crystalline nature of our system, which would require us to use unique values of  $c$  and  $\gamma$  for each mechanical mode depending on the direction of its motion with respect to the silicon crystal. Nonetheless, this calculation provides an estimate for the number of TLS defects interacting with each mechanical mode. It is worth noting that the calculated TLS densities for the second and third mechanical modes (6.28 MHz, 15.44 MHz) with larger  $V_{\text{str}}$  are very similar to the  $\sim 10^{21} \text{ m}^{-3}$  boron dopant density for the p-type silicon used to fabricate the devices, suggesting that these impurities are the cause of dissipation in these modes. We infer that the other two mechanical modes (3.53 MHz, 18.31 MHz) are coupled to TLS ensem-

bles comprised of defects created at the surface of the resonator during its fabrication [42]. These surface defects exhibit a smaller density than the boron impurities within the silicon because we have passivated dangling bonds at these exposed interfaces by performing an HF wet etch [43] as a final step in the device processing (see Methods).

### C. Two-Level System Contributions to Damping at High Temperature

As seen from extrapolations of the fits in Fig. 4, the mechanical damping due to TLS systems plateaus to a constant value  $\tilde{\Gamma}_{\text{TLS}}$  at high temperatures (see Supplementary Information). Therefore, one would expect that if the intrinsic mechanical damping rate is limited by coupling to TLS defects for  $T \gtrsim 10$  K, then the high temperature damping rate,  $\Gamma_{\text{HT}}$ , should be consistent with  $\Gamma_{\text{HT}} \approx \tilde{\Gamma}_{\text{TLS}} + \Gamma_{\text{p}}$ . To test this hypothesis, we have extracted  $\Gamma_{\text{HT}}$  from fits to the continuously measured spectra in Fig 1f-i, where optically induced heating significantly raises the temperature of the mechanical mode. Meanwhile,  $\Gamma_{\text{p}}$  is determined by fitting Eq. (3) to data similar to that seen in Fig. 3a at low temperatures ( $T \leq 500$  mK), where  $\Gamma_{\text{i}}$  is small enough that  $\Gamma \approx \Gamma_{\text{p}}$ . Comparing the values in Table II for each mechanical mode, we find that  $\Gamma_{\text{HT}} \approx \tilde{\Gamma}_{\text{TLS}} + \Gamma_{\text{p}}$  for the two mechanical modes with small  $V_{\text{str}}$ , suggesting that their intrinsic dissipation at high temperature is dominated by coupling to TLS defects. However, for the other two modes,  $\Gamma_{\text{HT}} > \tilde{\Gamma}_{\text{TLS}} + \Gamma_{\text{p}}$ , implying that another effect limits their dissipation at high temperature, likely a strain-dependent dissipation mechanism such as thermoelastic damping [41]. This again highlights the disparity between mechanical modes with small and large effective strain volumes.

### D. Radiation-Limited Damping and Decoherence Rates

We attribute the plateau in the damping rate below 100 mK, as characterized by  $\Gamma_0$ , to temperature-independent radiation of acoustic energy at the resonator's clamping points [34, 35]. This hypothesis is corroborated by observation of a smaller dissipation at low temperatures for mechanical devices with incorporated phononic shields [7, 33]. From  $\Gamma_0$ , we calculate the thermal decoherence rate,  $\Gamma_{\text{th}}$ , as well as decoherence time,  $\tau_{\text{th}} = 1/\Gamma_{\text{th}}$ , for each mechanical mode at the lowest measured temperature of 10 mK, the results for which are shown in Table II. We note that while these values are comparable with other state-of-the-art optomechanical devices measured at millikelvin temperatures [4, 7, 17, 33], these levels of mechanical decoherence are

only maintained for  $t < 1 \mu\text{s}$ , setting an upper bound on the time to perform coherent control operations.

### III. CONCLUSION

We have performed simultaneous optomechanical ringdown measurements for four mechanical modes in a single-crystal silicon nanomechanical resonator. Varying the temperature of the device, we have for the first time observed quantitative agreement between the standard tunneling model prediction for acoustic dissipation due to TLS defects in crystalline systems and the experimentally-determined damping rate for each of the transduced mechanical modes. We extract information about the energy distribution and density of the TLS defects, identifying them as p-type dopants for the mechanical modes with large effective strain volumes and surface defects for those exhibiting a small spread in their strain profile. Characterization of the TLS defects in this way provides a straightforward method by which we can decrease the low temperature dissipation in our devices simply by fabricating them from silicon with a reduced dopant level [39]. Further improvements to the cryogenic performance of our resonators may also be achieved by enhancing their quality via passivation and reconstruction of their surfaces in an  $\text{H}_2$  atmosphere [44]. Finally, by surrounding our device with a phononic crystal shield [45], it may be possible to reduce its damping rate even further, as radiation of acoustic energy into the substrate is the limiting dissipation mechanism at low temperatures. Application of the measurement technique used in this work to nanoresonators fabricated from other promising optomechanical materials, such as gallium arsenide [46] and diamond [47], will be the focus of future studies, as understanding the low temperature dissipation in these types of devices will be crucial for future applications in quantum information, such as quantum-coherent optical-to-microwave conversion [10, 11, 48], as well as quantum information processing and storage via interaction with nitrogen vacancy centers [49, 50].

### IV. METHODS

#### A. Device Fabrication

To fabricate our optomechanical devices, we start with a  $\langle 100 \rangle$  p-doped (boron,  $22.5 \Omega\cdot\text{cm}$ ) silicon-on-insulator (SOI) wafer, consisting of a 250 nm-thick device layer of monocrystalline sil-

icon on top of a 3  $\mu\text{m}$ -thick sacrificial layer of silicon dioxide supported by a 0.5 mm-thick silicon handle. The wafer is initially diced into 10 mm  $\times$  5 mm chips and cleaned using a hot piranha solution (75%  $\text{H}_2\text{SO}_4$ , 25%  $\text{H}_2\text{O}_2$ ) for 20 min. A masking layer (positive resist, ZEP-520a) is deposited onto the clean silicon device layer to pattern the half-ring/optical disk structure using a 30 kV e-beam lithography system (RAITH150 Two), followed by a cold development at  $-15^\circ\text{C}$  (ZED-N50). The chip is then reactive-ion etched ( $\text{C}_4\text{F}_8$  and  $\text{SF}_6$ ) to transfer the pattern to the silicon. The chip is subsequently cleaned with piranha and spun with a new mask (positive photoresist, HPR 504). After optical lithography, Cr and Au layers (7 nm and 210 nm, respectively) are sputtered on both sides of the chip with equal thickness, surrounding the devices with a gold thermalization layer, as shown in Fig. 1c. Ultrasonic lift-off in acetone and room-temperature piranha cleaning are then used to ensure cleanliness of these processed chips. Finally, the chips are immersed in HF solution (49% HF) for 1 minute to etch the sacrificial oxide layer, as well as passivate the exposed silicon surfaces of our devices [43], and are subsequently critical point dried to avoid stiction.

## B. Time-Resolved Balanced Homodyne Measurements of Mechanical Mode Occupancy

To perform measurements of the half-ring resonator’s mechanical mode occupancy, a gated homodyne detection scheme is implemented, as seen in Fig. 1a (see Supplementary Information for details). Light from a tunable diode laser (1550 – 1630 nm) is split into two branches: the local oscillator (LO) and the signal arm. By introducing a 200 MHz acousto-optic modulator (AOM) before the variable coupler (VC) that splits the input optical beam, both the signal and LO arms of the optical circuit can be gated with a  $\sim 5$  ns rise/fall time, permitting time-resolved optical measurements of the mechanical motion. In the signal arm, laser light travels into the dilution refrigerator where the relative position between a dimpled tapered fiber [51] and the sample is adjusted using a set of four linear positioning stages (Fig. 1b), allowing for evanescent coupling of light into, and subsequently out of, the microdisk’s optical modes, all while being monitored in real-time using a low temperature imaging system [37]. The laser wavelength is then tuned onto resonance with one of the microdisk’s optical whispering gallery modes at a frequency of  $\omega_c/2\pi = 188.8$  THz ( $\lambda_c = 1587.9$  nm) with optical linewidth  $\kappa/2\pi = 1.0$  GHz ( $Q_o = 1.9 \times 10^5$ ). Note that this choice of zero detuning ensures that optomechanical damping due to dynamical backaction can safely be ignored. The displacement of the half-ring resonator is dispersively

coupled to this optical mode, modulating its effective index of refraction, and therefore resonance frequency, such that the mechanical motion is encoded as a fluctuating phase of the optical signal that is transmitted through the cavity. Recombining this signal beam with the LO and measuring on a balanced photodetector (BPD), the mechanical motion is transduced into a time-varying voltage signal,  $v(t)$ , acquired using a fast (500 MS/s) analog-to-digital converter (ADC).

This signal is digitally analyzed in a way analogous to the output of a lock-in amplifier. That is, the time-series data is demodulated by multiplying by  $e^{-i\omega t}$ , as well as low-pass filtered (with a  $-3$  dB bandwidth of  $\sim 1.2$  MHz, time constant  $\tau_0 \approx 0.8 \mu\text{s}$ ) around the frequency of interest,  $\omega$ , via convolution with a Blackman window,  $H(t)$ . Mathematically, this is interpreted as the “band-passed” Fourier transform

$$\mathcal{V}(\omega, t) = \int_{-\infty}^{\infty} v(t - t') e^{-i\omega(t-t')} H(t') dt', \quad (6)$$

performed at each time step,  $t$ , of the ADC signal. Note that the  $\sim 1.2$  MHz bandwidth of the filter function is much larger than the linewidth of any of the studied mechanical modes, ensuring that the entire area of each considered resonance peak will be encapsulated. Furthermore, while the data is taken with a time step of 2 ns, we are unable to resolve features that evolve faster than the  $0.8 \mu\text{s}$  time constant set by this bandwidth.

From the Fourier transform in Eq. (6), we can determine the time-resolved, “band-passed” power spectral density of  $v(t)$  as

$$S_v(\omega, t) = \frac{|\mathcal{V}(\omega, t)|^2}{\tau_0}. \quad (7)$$

If we choose our demodulation frequency to be equal to one of our mechanical resonances (*i.e.*  $\omega = \omega_m$ ), the quantity in Eq. (7) will be proportional to the energy stored in that mode, providing a direct measure of its phonon occupancy in the high temperature limit as  $\langle n \rangle (t) \approx k_B T_m(t) / \hbar \omega_m \propto S_x(\omega_m, t) \propto S_v(\omega_m, t)$ , where  $S_x(\omega, t)$  is the “band-passed” power spectral density of the mechanical mode’s displacement,  $x(t)$ , and  $T_m(t)$  is the time-dependent mechanical mode temperature (see Supplementary Information).

- 
- [1] O'Connell, A. D. *et al.* Quantum ground state and single-phonon control of a mechanical resonator. *Nature* **464**, 697-703 (2010).
- [2] Teufel, J. D. *et al.* Sideband cooling of micromechanical motion to the quantum ground state. *Nature* **475**, 359-363 (2011).
- [3] Chan, J. *et al.* Laser cooling of a nanomechanical oscillator into its quantum ground state. *Nature* **478**, 89-92 (2011).
- [4] Wollman, E. E. *et al.* Quantum squeezing of motion in a mechanical resonator. *Science* **349**, 952-955 (2015).
- [5] Pirkkalainen, J.-M., Damskäg, E., Brandt, M., Massel, F. & Sillanpää, M. A. Squeezing of quantum noise of motion in a micromechanical resonator. *Phys. Rev. Lett.* **115**, 243601 (2015).
- [6] Palomaki, T. A., Teufel, J. D., Simmonds, R. W. & Lehnert, K. W. Entangling mechanical motion with microwave fields. *Science* **342**, 710-713 (2013).
- [7] Riedinger, R. *et al.* Non-classical correlations between single photons and phonons from a mechanical oscillator. *Nature* **530**, 313-316 (2016).
- [8] Reed, A. P. *et al.* Faithful conversion of propagating quantum information to mechanical motion. *Nat. Phys.* Advanced Online Publication (2017).
- [9] Hill, J. T., Safavi-Naeini, A. H., Chan, J. & Painter, O. Coherent optical wavelength conversion via cavity optomechanics. *Nat. Comm.* **3**, 1196 (2012).
- [10] Bochmann, J., Vainsencher, A., Awschalom, D. D. & Cleland, A. N. Nanomechanical coupling between microwave and optical photons. *Nat. Phys.* **9**, 712-716 (2013).
- [11] Andrews, R. W. *et al.* Bidirectional and efficient conversion between microwave and optical light. *Nat. Phys.* **10**, 321-326 (2014).
- [12] Teufel, J. D., Donner, T., Castellanos-Beltran, M. A., Harlow, J. W. & Lehnert, K. W. Nanomechanical motion measured with an imprecision below that at the standard quantum limit. *Nat. Nano.* **4**, 820-823 (2009).
- [13] Kim, P. H., Hauer, B. D., Doolin, C., Souris, F. & Davis, J. Approaching the standard quantum limit of mechanical torque sensing. *Nat. Comm.* **7**, 13165 (2016).
- [14] Stannigel, K. *et al.* Optomechanical quantum information processing with photons and phonons. *Phys. Rev. Lett.* **109**, 013603 (2012).

- [15] Wang, Y.-D. & Clerk, A. A. Using interference for high fidelity quantum state transfer in optomechanics. *Phys. Rev. Lett.* **108**, 153603 (2012).
- [16] Verhagen, E., Deléglise, S., Weis, S., Schliesser, A. & Kippenberg, T. J. Quantum-coherent coupling of a mechanical oscillator to an optical cavity mode. *Nature* **482**, 63-67 (2012).
- [17] Palomaki, T. A., Harlow, J. W., Teufel, J. D., Simmonds, R. W. & Lehnert, K. W. Coherent state transfer between itinerant microwave fields and a mechanical oscillator. *Nature* **495**, 210-214 (2013).
- [18] Aspelmeyer, M., Kippenberg, T. J. & Marquardt, F. Cavity optomechanics. *Rev. Mod. Phys.* **86**, 1391-1452 (2014).
- [19] Mohanty, P. *et al.* Intrinsic dissipation in high-frequency micromechanical resonators. *Phys. Rev. B* **66**, 085416 (2002).
- [20] Phillips, W. A. Two-level states in glasses. *Rep. Prog. Phys.* **50**, 1657-1708 (1987).
- [21] Pohl, R. O., Liu, X. & Thompson, E. Low-temperature thermal conductivity and acoustic attenuation in amorphous solids. *Rev. Mod. Phys.* **74**, 991-1013 (2002).
- [22] Phillips, W. A. *Phys. Rev. Lett.* **61**, 2632 (1988).
- [23] Kleiman, R. N., Agnolet, G. & Bishop, D. J. Two-level systems observed in the mechanical properties of single-crystal silicon at low temperatures. *Phys. Rev. Lett.* **59**, 2079-2082 (1987).
- [24] Mihailovich, R. E. & Parpia, J. M. Anomalous low temperature mechanical properties of single-crystal silicon. *Physica B* **165/166**, 125-126 (1990).
- [25] Zolfagharkhani, G., Gaidarzhy, A., Shim, S.-B., Badzey, R. L. & Mohanty, P. Quantum friction in nanomechanical oscillators at millikelvin temperatures. *Phys. Rev. B* **72**, 224101 (2005).
- [26] Shim, S. B. *et al.* Micromechanical resonators fabricated from lattice-matched and etch-selective GaAs/InGaP/GaAs heterostructures. *Appl. Phys. Lett.* **91**, 133505 (2007).
- [27] Imboden, M. & Mohanty, P. Evidence of universality in the dynamical response of micromechanical diamond resonators at millikelvin temperatures. *Phys. Rev. B* **79**, 125424 (2009).
- [28] Hüttel, A. K. *et al.* Carbon nanotubes as ultrahigh quality factor mechanical resonators. *Nano. Lett.* **9**, 2547-2552 (2009).
- [29] Goryachev, M. *et al.* Extremely low-loss acoustic phonons in a quartz bulk acoustic wave resonator at millikelvin temperature. *Appl. Phys. Lett.* **100**, 243504 (2012).
- [30] Ahn, K.-H. & Mohanty, P. Quantum friction of micromechanical resonators at low temperatures. *Phys. Rev. Lett.* **90**, 085504 (2003).
- [31] Jiang, H., Yu, M.-F., Liu, B. & Huang, Y. Intrinsic energy loss mechanisms in a cantilevered carbon

- nanotube beam oscillator. *Phys. Rev. Lett.* **93**, 185501 (2004).
- [32] Seoáñez, C., Guinea, F. & Castro Neto A. H. Surface dissipation in nanoelectromechanical systems: unified description with the standard tunneling model and effects of metallic electrodes. *Phys. Rev. B* **77**, 125107 (2008).
- [33] Meenehan, S. M. *et al.* Pulsed excitation dynamics of an optomechanical crystal resonator near its quantum ground state of motion. *Phys. Rev. X* **5**, 041002 (2015).
- [34] Cross, M. C. & Lifshitz, R. Elastic wave transmission at an abrupt junction in a thin plate with applications to heat transport and vibrations in mesoscopic systems. *Phys. Rev. B* **64**, 085324 (2001).
- [35] Wilson-Rae, I. Intrinsic dissipation in nanomechanical resonators due to phonon tunneling. *Phys. Rev. B* **77**, 245418 (2008).
- [36] Holland, M. G. Analysis of lattice thermal conductivity. *Phys. Rev.* **132**, 2461-2471 (1963).
- [37] MacDonald, A. J. R. *et al.* Optical microscope and tapered fiber coupling apparatus for a dilution refrigerator. *Rev. Sci. Instrum.* **86**, 013107 (2015).
- [38] Fjeldy, T., Ishiguro, T. & Elbaum, C. Heat-pulse propagation in *p*-type Si and Ge under uniaxial stress. *Phys. Rev. B* **7**, 1392-1410 (1973).
- [39] Mihailovich, R. E. & Parpia, J. M. Low temperature mechanical properties of boron-doped silicon. *Phys. Rev. Lett.* **68**, 3052-3055 (1992).
- [40] Hauer, B. D., Doolin, C., Beach, K. S. D. & Davis, J. P. A general procedure for thermomechanical calibration of nano/micro-mechanical resonators. *Ann. Phys.* **339**, 181-207 (2013).
- [41] Lifshitz, R. & Roukes, M. L. Thermoelastic damping in micro- and nanomechanical systems. *Phys. Rev. B* **61**, 5600-5609 (2000).
- [42] Borselli, M., Johnson, T. J. & Painter, O. Measuring the role of surface chemistry in silicon microphonics. *Appl. Phys. Lett.* **88**, 131114 (2006).
- [43] Higashi, G. S., Chabal, Y. J., Trucks, G. W. & Raghavachari K. Ideal hydrogen termination of the Si (111) surface. *Appl. Phys. Lett.* **56**, 656-658 (1990).
- [44] Bender, H., Verhaverbeke, S., Caymax, M., Vatel, O. & Heyns, M. M. Surface reconstruction of hydrogen annealed (100) silicon. *J. Appl. Phys.* **75**, 1207-1209 (1994).
- [45] Alegre, T. P. M., Safavi-Naeini, A., Winger, M. & Painter, O. Quasi-two-dimensional optomechanical crystals with a complete phononic bandgap. *Opt. Express* **19**, 5658-5669 (2011).
- [46] Balram, K. C., Davanço, M. I., Song, J. D. & Srinivasan, K. Coherent coupling between radiofrequency, optical and acoustic waves in piezo-optomechanical circuits. *Nat. Photon.* **10**, 346-352 (2016).

- [47] Mitchell, M. *et al.* Single-crystal diamond low-dissipation cavity optomechanics. *Optica* **3**, 963-970 (2016).
- [48] Whitmer, J. D. *et al.* High-Q photonic resonators and electro-optic coupling using silicon-on-lithium-niobate. *Sci. Rep.* **7** 46313 (2017).
- [49] Golter, D. A., Oo, T., Amezcua, M., Stewart, K. A. & Wang, H. Optomechanical quantum control of a nitrogen-vacancy center in diamond. *Phys. Rev. Lett.* **116**, 143602 (2016).
- [50] Arcizet, O. *et al.* A single nitrogen-vacancy defect coupled to a nanomechanical oscillator. *Nat. Phys.* **7**, 879-883 (2011).
- [51] Hauer, B. D. *et al.* On-chip cavity optomechanical coupling. *EPJ Tech. Instrum.* **1**:4 (2014).

## V. ACKNOWLEDGEMENTS

This work was supported by the University of Alberta, Faculty of Science; the Natural Sciences and Engineering Research Council, Canada (Grants Nos. RGPIN-2016-04523, DAS492947-2016, and STPGP 493807 - 16); and the Canada Foundation for Innovation. B.D.H. acknowledges support from the Killam Trusts.

## VI. AUTHOR CONTRIBUTIONS

B.D.H., P.H.K., C.D., F.S., and J.P.D. conceived, designed, and maintained the experiment. B.D.H. and C.D. developed the data taking procedure. B.D.H. acquired all data. B.D.H., C.D., and F.S. analyzed the data. B.D.H. performed all simulations. P.H.K. nanofabricated the devices studied. B.D.H., P.H.K., C.D., and J.P.D. wrote the manuscript. All authors contributed to manuscript and figure editing.

## VII. COMPETING FINANCIAL INTERESTS

The authors declare no competing financial interests.

# Supplementary Information for Two-Level System Damping in a Single-Crystal Silicon Optomechanical Resonator

## S1. EXPERIMENTAL DETAILS

### A. Gated Homodyne Measurement

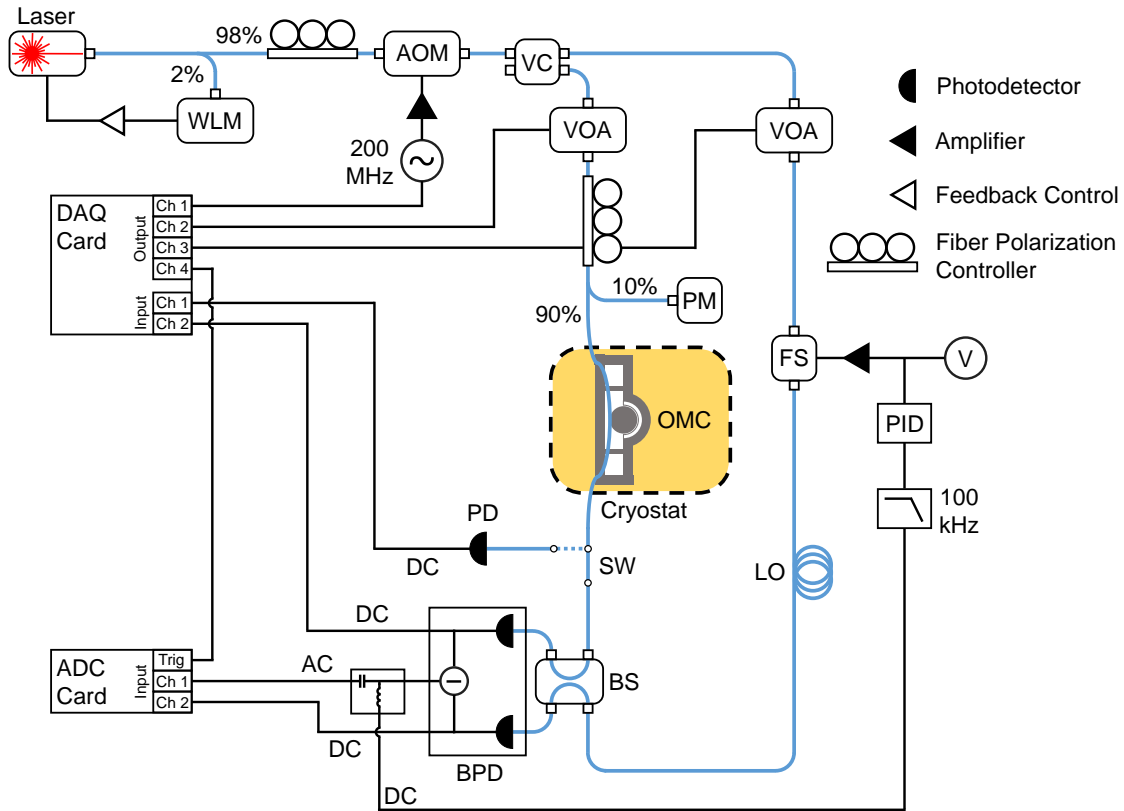


FIG. S1. **Experimental setup.** Detailed schematic of the gated homodyne detection system used to perform measurements of the cryogenic optomechanical device presented in the main text. WLM = wavelength meter, AOM = acousto-optic modulator, VC = variable coupler, VOA = variable optical attenuator, PM = power meter, FS = fiber stretcher, PID = proportional-integral-derivative controller, V = voltmeter, LO = local oscillator, SW = optical switch, BS = beam splitter, BPD = balanced photodetector, PD = photodetector, ADC = analog-to-digital converter, DAQ = data acquisition.

To measure the motion of our optomechanical device, we implemented a gated optical homodyne detection scheme, a detailed schematic of which can be seen in Fig. S1. Light from a tunable external cavity diode laser is fiber coupled into the optical circuit, where its wavelength is monitored using a 2% pick-off to a wavelength meter (WLM), with this reading fed back into the laser

controller to ensure long-term frequency stability. The remainder of the signal is sent through an acousto-optic modulator (AOM), allowing for gating of the optical signal with a rise/fall time of  $\sim 5$  ns, faster than all other timescales associated with the system. The laser light is then sent through a variable coupler, where it is split into two separate beams: the signal and the local oscillator (LO), with the power in each arm set by a voltage-controlled variable optical attenuator (VOA). For the measurements detailed in the main text, the LO is kept at a constant power of 2.6 mW, while the power in the signal arm is varied depending on the experiment. The light in the signal arm is coupled into and out of the dilution unit using optical fiber feedthroughs, with its polarization optimized using a fiber polarization controller (FPC) and its power monitored by a power meter (PM). Inside the fridge, a low-temperature dimpled tapered fiber is used to inject light into the optomechanical device, while also collecting the optical signal exiting the cavity. After coupling out of the fridge, this optical signal is recombined with the LO via a 50/50 fiber beam splitter (BS), with both outputs sent to a balanced photodetector (BPD). The path length difference between the LO and signal arm of the circuit is maintained by feeding the DC voltage difference signal of the BPD through a proportional-integral-derivative (PID) controller and into a fiber stretcher (FS), such that fluctuations from the setpoint of the optical path length are compensated for in the LO arm. This process locks the phase of the homodyne measurement and allows for probing of a specific quadrature of the optical field, extracting the mechanical motion as fluctuations in the AC portion of the BPD's voltage difference signal, which is recorded in the time domain using a 500 MS/s analog-to-digital converter (ADC). The DC voltage readouts from each of the BPD's individual photodetectors are also collected, with one output sent to a low-frequency data acquisition (DAQ) card to monitor slow drifts, while the other is sent to the ADC to observe rapid transients in this signal. Finally, we note that we have included a voltage-controlled optical switch (SW) after the fiber output from the fridge, such that we can opt to toggle the optical signal out of the homodyne loop to a standard photodetector (PD), allowing for DC monitoring of transmission through the optical cavity, and thus, its lineshape.

To perform the pulsed measurements described in the main text, the optomechanical detection system is initially set up by sending a continuous-wave laser signal through the optical circuit. The dimpled tapered fiber is then carefully aligned to couple with the microdisk, after which the laser wavelength is tuned onto resonance with one of the cavity's optical modes and the transduction of the mechanical signal is optimized. We note that due to the relatively high optical powers (10 – 100  $\mu$ W) input to the fridge during this initial set up, the base plate, along with the optomechanical

device, heats up significantly. Therefore, once we have ensured that the fiber is in place, the optical circuit is toggled into the “off” state by closing the AOM (extinction ratio of 50 dB), preventing optical power from reaching the dimple. After approximately 1 – 2 hours in this state, the fridge returns to its initial temperature and is ready for pulsing measurements.

For the double pulse measurement outlined in the inset of Fig. 3a of the main text, we begin by sending a trigger signal from Output Ch 1 of the DAQ card to a 200 MHz frequency source, activating an output signal that is amplified to  $10 V_{\text{RMS}}$  and sent to the AOM. This electrical signal opens the AOM, generating the initial pump pulse that is used to thermally excite the motion of the mechanical resonator. The AOM is left open until the predetermined pulse time,  $t_1$ , has passed, at which point it is closed by turning the frequency source off with a second signal from the DAQ card. The mechanical resonator is then left in the dark to decay towards thermal equilibrium for a set wait time,  $t_{\text{off}}$ , after which a probe pulse, created in an identical manner to the pump pulse, is sent to access the device. To ensure the data from the probe pulse is recorded, the ADC is activated using another trigger signal generated by Output Ch 4 of the DAQ card at a time chosen to be 10 or 100  $\mu\text{s}$  – depending on the length  $t_{\text{off}}$  – before the probe pulse is created. Finally, the AOM is triggered off after a time,  $t_2$ , has elapsed following the generation of the probe pulse, returning the optical circuit back to its “off” state. Note that for the experiments performed here, we always take  $t_1 = t_2$ , such that the phonon occupation of the mechanical mode at the end of the pump pulse can be inferred from observation of the probe pulse (see Section S7), minimizing the amount of data that needs to be collected. After a 200 ms wait to reinitialize the ADC, this procedure is repeated until the desired number of pulses is acquired. Single pulse measurements are performed identically to the double pulse measurements, with the omission of the pump pulse. We note that the gating of the optical circuit is completely controlled by outputs from the DAQ card, ensuring consistent timing referenced to its 1 MHz internal clock.

## B. Optomechanical Detection Efficiency

To determine the efficiency of our optomechanical detection, we analyze the losses at each juncture of our optical circuit. While coupling to the device, light from the tapered optical fiber is scattered off the substrate, as well as lost as photons travel through the fiber and out of the fridge, with corresponding transmission efficiencies of  $\eta_s = 62.6\%$  and  $\eta_f = 72.0\%$ , respectively. Further losses in the fiber at room temperature result in a fraction  $\eta_{\text{RT}} = 81.6\%$  of the light that exits the

fridge reaching the BPD. Including the quantum efficiency of the BPD itself,  $\eta_{\text{BPD}} = 78.1\%$ , the total optomechanical detection efficiency of the system (*i.e.* the fraction of photons coupled out of the device that are converted into measured photoelectrons) is given by  $\eta = \eta_s \eta_f \eta_{\text{RT}} \eta_{\text{BPD}} = 30.3\%$ .

### C. Thermometry and Temperature Control

To measure the temperature of the base plate of the dilution refrigerator, two complementary thermometers are used. The counts of gamma ray emission from a  $^{60}\text{Co}$  nuclear orientation (NO) thermometer over a 570 s time window, referenced to a high temperature count rate at 4.2 K, provided accurate temperature readings below 50 mK, while the resistance curve of a RuO thermometer is used for  $T \geq 50$  mK. Uncertainty in the temperature readings of the NO thermometer are obtained as the standard deviation in the spread of reported temperatures over the course of a measurement, while the RuO error is taken as the uncertainty in the accuracy of the sensor as specified by the supplier.

In order to heat the dilution refrigerator above its base temperature of 10 mK, current is applied to a resistive heater mounted on the mixing chamber plate, with temperature stability for the duration of a given measurement ensured by a PID-controlled feedback loop referenced to the RuO thermometer. In the range of 10 mK to 800 mK, the cooling power is provided by operating the dilution unit, while for temperatures up to 4.2 K, fridge circulation is ceased and cooling is supplied by the 1K pot. Finally, above 4.2 K, the 1K pot is stopped, such that connection to the liquid helium bath surrounding the fridge is the source of cooling for the base plate.

## S2. OPTOMECHANICAL DEVICE

The studied optomechanical device, as seen in Fig. 1c,d of the main text, is comprised of a suspended half-ring mechanical resonator side-coupled to a  $10 \mu\text{m}$  diameter optical microdisk cavity, separated by a vacuum gap of 75 nm. The microdisk cavity supports a number of optical whispering gallery modes, each at a frequency  $\omega_c$ , characterized by an electric field profile  $\vec{\mathcal{E}}(\vec{r}, t) = \mathcal{E}(t)\vec{w}(\vec{r})$  [S1]. Likewise, the motion of the half-ring resonator can be broken down into a set of mechanical modes at frequency  $\omega_m$ , described by their displacement from equilibrium  $\vec{u}(\vec{r}, t) = x(t)\vec{q}(\vec{r})$  [S1, S2]. Here, we have separated both the electric field and displacement

profiles into their time-dependent amplitudes,  $\mathcal{E}(t)$  and  $x(t)$ , with their spatially-varying modeshapes,  $\vec{w}(\vec{r})$  and  $\vec{q}(\vec{r})$ , normalized such that  $\max|\sqrt{\epsilon(\vec{r})}\vec{w}(\vec{r})| = \max|\vec{q}(\vec{r})| = 1$ . In this way, we can characterize the spatial extent of the optical mode through the effective mode volume,  $V_{\text{opt}} = \int \epsilon(\vec{r})|\vec{\mathcal{E}}(\vec{r})|^2 dV$  [S1, S3], as well as the extended nature of the mechanical resonator via an effective mass,  $m_{\text{eff}} = \int \rho(\vec{r})|\vec{q}(\vec{r})|^2 dV$  [S1, S2]. Each of these integrals are performed over the volume of the entire optomechanical system, where  $\epsilon(\vec{r})$  and  $\rho(\vec{r})$  are the dielectric profile and mass density of the device.

Dispersive optomechanical coupling is realized between these optical and mechanical degrees of freedom due to the fact that the motion of the half-ring resonator perturbs the boundaries of the microdisk cavity, shifting the resonant frequencies of its optical modes. To first order, these shifts can be expressed as  $\omega_c(x(t)) \approx \omega_c + Gx(t)$ , where  $G = d\omega_c/dx$  is the optomechanical coupling coefficient. Using a perturbative approach [S1, S4], an expression for  $G$  can be found as

$$G = \frac{\omega_c}{2V_{\text{opt}}} \int \vec{q}(\vec{r}) \cdot \hat{n}(\vec{r}) [\Delta\epsilon|\vec{w}_{\parallel}(\vec{r})|^2 - \Delta\epsilon^{-1}\epsilon^2(\vec{r})|\vec{w}_{\perp}(\vec{r})|^2] dA, \quad (\text{S1})$$

where the integration is performed over the surface of the mechanical resonator. Here,  $\vec{w}_{\parallel}(\vec{r})$  and  $\vec{w}_{\perp}(\vec{r})$  are the components of  $\vec{w}(\vec{r})$  parallel and perpendicular to the surface of the mechanical resonator, as defined by its spatially-varying unit normal vector  $\hat{n}(\vec{r})$ , with  $\Delta\epsilon = \epsilon_{\text{d}} - \epsilon_{\text{m}}$  and  $\Delta\epsilon^{-1} = \epsilon_{\text{d}}^{-1} - \epsilon_{\text{m}}^{-1}$  defined in terms of the permittivities of the device's material,  $\epsilon_{\text{d}}$ , and surrounding medium,  $\epsilon_{\text{m}}$ . We also introduce the single photon, single phonon optomechanical coupling rate,  $g_0 = Gx_{\text{zpf}}$ , which corresponds to the shift in the optical cavity's resonance frequency due to the fluctuation amplitude of the resonator's zero-point motion,  $x_{\text{zpf}} = \sqrt{\hbar/2\omega_{\text{m}}m_{\text{eff}}}$  (*i.e.* the root-mean-square value of  $x(t)$  when the mechanical resonator is in its ground state).

For the measurements performed in the main text, we measure the motion of the mechanical modes shown in Fig. 1f-i using the first order radial mode of the optomechanical cavity (azimuthal mode number  $M = 49$  – see Fig. 1d), with resonant frequency  $\omega_c/2\pi = 188.8$  THz ( $\lambda_c = 1587.9$  nm) and linewidth  $\kappa/2\pi = 1.0$  GHz ( $Q_{\text{o}} = 1.9 \times 10^5$ ). Due to optical heating of the mechanical mode, as well as an anomalous optomechanical damping effect that will be the subject of future studies, it is difficult to obtain an experimentally-determined value of  $G$ . However, by performing finite element method (FEM) simulations of the optical and mechanical modeshapes of the device, we can calculate  $G$  for the device according to Eq. (S1). As well, we use the simulated mechanical modeshape to determine  $m_{\text{eff}}$ , from which we can find  $x_{\text{zpf}}$ , and subsequently,  $g_0$ .

These values for each mechanical mode are found in Table S1. We note that due to the symmetry of the displacement with respect to the optical field, we simulate  $G \approx 0$  for the two lower frequency mechanical modes, even though this symmetry is broken in the experiment, such that significant optomechanical coupling exists.

$\omega_m/2\pi$ (MHz)	$m_{\text{eff}}$ (fg)	$x_{\text{zpf}}$ (fm)	$G/2\pi$ (GHz/nm)	$g_0/2\pi$ (kHz)
3.53	610	62.4	–	–
6.28	836	40.0	–	–
15.44	743	27.0	2.34	63.4
18.31	772	24.4	5.13	125

TABLE S1. Summary of the optomechanical properties for each mechanical mode. The effective mass,  $m_{\text{eff}}$ , and optomechanical coupling coefficient,  $G$ , are determined using FEM simulations for the electric field and displacement profiles of the optomechanical device. From these values, the zero-point fluctuation amplitude,  $x_{\text{zpf}}$ , and the single-photon optomechanical coupling rate,  $g_0$ , are calculated. Note that due to the symmetry of the simulated system, the values of  $G$  given here represent a lower bound for the considered geometry and are only nonzero for the two higher frequency mechanical modes.

### S3. CALIBRATION OF MECHANICAL MODE TEMPERATURE

The measured signal in our experiment is a fluctuating voltage,  $v(t)$ , at the output of a balanced photodetector, which encodes the mechanical motion of our device (see Section S1 A). Transforming this signal into the frequency domain, we obtain its single-sided, “band-passed” spectral density function (see Methods), which will in general be given by

$$S_v(\omega, t) = \sum_i \alpha_i(\omega, t) S_x^i(\omega, t) + S_v^{\text{imp}}(\omega), \quad (\text{S2})$$

where  $\alpha_i(\omega, t)$  is the transduction coefficient for the single-sided, “band-passed” displacement spectral density  $S_x^i(\omega, t)$  corresponding to the  $i$ th mechanical mode of the resonator and  $S_v^{\text{imp}}(\omega)$  is the frequency-dependent imprecision noise floor of the measurement. In general, the coefficients  $\alpha_i(\omega, t)$  are a combination of a number of experimental parameters and difficult to determine *a priori*. We therefore look for a simple way to relate the spectral density of our measurement to the temperature of the mode in question.

If we consider a finite bandwidth,  $\Delta\omega$ , surrounding the resonance frequency of a single me-

chanical mode, the sum in Eq. (S2) collapses and we can approximate the transduction coefficient and noise floor as constant over this frequency range. Furthermore, the time-dependence in  $\alpha(\omega, t)$  is due to the ring-up of the optical cavity, which occurs on a timescale of  $1/\kappa \approx 1$  ns, which is much faster than any other component in our detection system. We can therefore treat  $\alpha(\omega, t)$  as a step function in time, such that it takes on a constant value once the laser reaches the optical cavity. We then have  $\sum_i \alpha_i(\omega, t) S_x^i(\omega, t) \approx \alpha S_x(\omega, t)$  and  $S_v^{\text{imp}}(\omega) \approx S_v^{\text{imp}}$  such that

$$S_v(\omega, t) \approx \alpha S_x(\omega, t) + S_v^{\text{imp}}, \quad (\text{S3})$$

where  $S_x(\omega, t)$  is the displacement spectral density of the mechanical mode we are interested in. This signal can be related to the time-dependent temperature,  $T_m(t)$ , of the mechanical mode using the expression [S5]

$$\int S_x(\omega, t) d\omega \approx \frac{4\pi x_{\text{zpf}}^2 k_B}{\hbar \omega_m} T_m(t) = \frac{\pi}{2} \Gamma S_x(\omega_m, t), \quad (\text{S4})$$

where the integration is performed over the bandwidth  $\Delta\omega$  centered on  $\omega_m$  and we have assumed the experimentally-relevant high-temperature regime (*i.e.*  $k_B T_m(t) \gg \hbar \omega_m$  for all  $t$ ). Combining Eq. (S4) with Eq. (S3), we find that

$$\int S_v(\omega, t) d\omega = \xi T_m(t) + \mu, \quad (\text{S5})$$

indicating that the area under the curve of the measured voltage spectral density is linearly related to the mechanical mode temperature, with proportionality  $\xi = 4\pi x_{\text{zpf}}^2 k_B \alpha / \hbar \omega_m$  and a constant offset  $\mu = S_v^{\text{imp}} \Delta\omega$  set by the noise floor and bandwidth of the measurement. Fitting Eq. (S5) to the area under the voltage spectral density at the beginning of the pulse, when the mechanical mode is thermalized to the fridge temperature,  $T$ , at  $t = t_0$  allows us to infer the initial mode temperature as  $T_m(t_0) = T$  and extract values for  $\beta$  and  $\eta$ . Provided the conditions stay the same throughout the experiment, we can use these parameters to determine the mode temperatures at later times in the pulse as the device rapidly heats due to absorption of photons from the optical cavity. An example of this type of calibration is seen in Fig. 2 of the main text.

#### S4. STANDARD TUNNELING MODEL FOR ACOUSTIC DAMPING IN CRYSTALLINE SOLIDS

In the early 1970's, it was discovered by Zeller and Pohl [S6] that the cryogenic thermal properties of a number of glassy solids deviated significantly from what was expected according to the Debye model. To account for this anomalous behaviour, Anderson *et al.* [S7] and Phillips [S8] simultaneously developed what is now known as the standard tunneling model (STM), whereby phonons in the solid exchange energy with the medium by driving configurational changes of intrinsic defect states. Further extensions to this model were made by Jäckle *et al.* [S9, S10], who used it to correctly describe anomalous acoustic absorption observed in fused quartz [S11]. While early incarnations of the STM were used with great success to describe the cryogenic properties of amorphous solids, it was not until similar anomalies were observed in the acoustic dissipation and dispersion of single crystal silicon mechanical resonators [S12, S13] that a method was proposed by Phillips [S14] to broaden the STM to include crystalline solids.

In this section, we provide an overview of the STM in the general form originally used to describe amorphous solids, and extend it to describe mechanical dissipation in crystalline materials according to the model postulated by Phillips [S14].

##### A. Double-Well Potential Model for Tunneling Systems

In the STM, the configurational states of the defects in the solid are modelled as a particle of mass  $m$  confined to an asymmetric double-well potential [S7, S8], as seen in Fig. S2. We assume this potential to be comprised of two identical harmonic wells, each with a ground state energy,  $E_0 = \hbar\Omega/2$ , offset by an asymmetry energy,  $\Delta$ , and separated by a barrier of height,  $B$ , and the configurational coordinate,  $d$ . We consider the system to be at low enough temperatures ( $k_B T \ll \hbar\Omega$ ) such that only the ground state of each well will be populated with any significant probability. This allows for a two-level system (TLS) description of these two lowest lying configurational states, with wavefunctions  $\psi_L(\vec{r})$  ( $\psi_R(\vec{r})$ ) corresponding to the particle occupying the higher (lower) energy state in the left (right) well. In this set of localized basis states, the Hamiltonian will be given by [S15, S16]

$$\mathcal{H}_0 = \frac{1}{2} \begin{bmatrix} \Delta & -\Delta_0 \\ -\Delta_0 & -\Delta \end{bmatrix}, \quad (\text{S6})$$

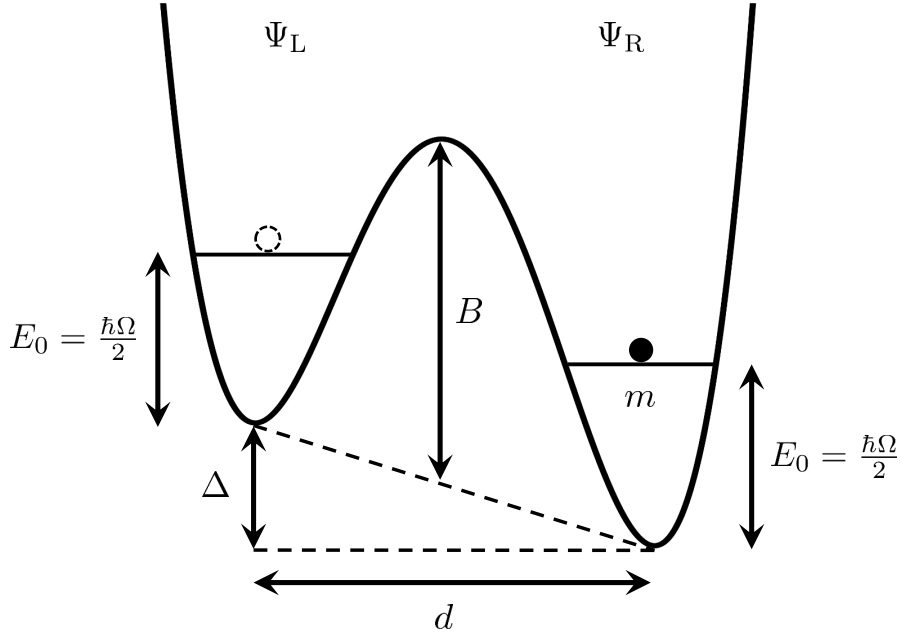


FIG. S2. **Tunneling in a double-well potential.** Schematic of a particle of mass,  $m$ , tunneling between the two ground states of a double-well potential, separated by a barrier height,  $B$ , and a coordinate,  $d$ , with an asymmetry,  $\Delta$ , between their two minima. The particle can tunnel through the barrier, allowing it to be localized in the ground state of either the left or right well (each with energy  $E_0 = \hbar\Omega/2$ ), as described by the wavefunctions  $\psi_L$  and  $\psi_R$ , respectively.

where we have chosen zero energy to be the midway point between the minimum of each well. In this Hamiltonian, quantum tunneling between the two states of the TLS is characterized by the “tunnel splitting” or “tunneling energy”,  $\Delta_0$ , which can be determined using the Wentzel-Kramers-Brillouin (WKB) approximation to be  $\Delta_0 \approx \hbar\Omega e^{-\lambda}$ , where  $\lambda = \sqrt{2mBd^2/\hbar^2}$  is known as the “tunneling” or “Gamow” parameter and characterizes the penetration of the wavefunctions into the barrier [S15].

The Hamiltonian in Eq. (S6) can be diagonalized by rotating the basis by an angle  $\phi$  defined by  $\tan(2\phi) = \Delta_0/\Delta$ , resulting in the new Hamiltonian [S15, S16]

$$H_0 = \frac{1}{2} \begin{bmatrix} E & 0 \\ 0 & -E \end{bmatrix}, \quad (\text{S7})$$

in the energy eigenstate basis

$$\begin{aligned}\psi_+(\vec{r}) &= \psi_L(\vec{r}) \cos(\phi) - \psi_R(\vec{r}) \sin(\phi), \\ \psi_-(\vec{r}) &= \psi_L(\vec{r}) \sin(\phi) + \psi_R(\vec{r}) \cos(\phi).\end{aligned}\tag{S8}$$

Here,  $E = \sqrt{\Delta^2 + \Delta_0^2}$  is the energy separation between the two states of the TLS, with the wavefunctions  $\psi_{\pm}(\vec{r})$  corresponding to the eigenvalues  $\pm E/2$ . If the TLS is in thermal equilibrium at a temperature,  $T$ , we can use the diagonalized Hamiltonian of Eq. (S7) to determine the probability that the TLS is in either of its two states as

$$p_{\pm}^0 = \frac{e^{\mp E/2k_B T}}{e^{E/2k_B T} + e^{-E/2k_B T}} = \frac{1}{e^{\pm E/k_B T} + 1},\tag{S9}$$

with  $p_+^0$  ( $p_-^0$ ) corresponding to the excited (ground) state. From these equilibrium probabilities, we can also determine the contribution to the internal energy of the system due to an ensemble of  $N$  TLS as

$$U = Np_+^0 \frac{E}{2} - Np_-^0 \frac{E}{2} = NE \left( p_+^0 - \frac{1}{2} \right).\tag{S10}$$

Note that the addition of  $E/2$  per TLS arises due to our choice of zero energy.

## B. Phononic Perturbations

Tunneling systems that are embedded in a solid are able to exchange energy with the various excitations of the surrounding medium. Here, we focus on insulating solids, such that the dominant excitation at low temperatures will be quantized vibrations of the lattice, *i.e.* phonons. If the interacting phonon has energy on the order of, or greater than, the TLS separation energy, it can be directly absorbed, promoting a TLS in its ground state to its excited state. However, for single-crystal silicon, the TLS separation energies correspond to GHz frequencies (or higher) [S12, S17], such that this resonant interaction does not need to be considered for the MHz frequency mechanical modes studied in this work. Instead, we focus on another TLS-phonon interaction, known as the relaxation interaction [S15, S16, S18], whereby non-resonant phonons generate strains that perturb the local TLS environment, driving the system out of thermal equilibrium by shifting the energy separation between their two levels. This causes the TLS to interact with the vibrational modes of the solid, absorbing and emitting phonons until it can relax back to thermal equilibrium.

To model this relaxation effect, we introduce the perturbation Hamiltonian [S16, S18]

$$\mathcal{H}' = \frac{1}{2} \begin{bmatrix} \Delta'(t) & 0 \\ 0 & -\Delta'(t) \end{bmatrix}, \quad (\text{S11})$$

which can be transformed into the energy eigenbasis to obtain

$$H' = \frac{1}{E} \begin{bmatrix} \Delta & \Delta_0 \\ \Delta_0 & -\Delta \end{bmatrix} \gamma \varepsilon(t). \quad (\text{S12})$$

Here,  $\Delta'(t) = 2\gamma\varepsilon(t)$  is the shift in energy due to the time-dependent, phonon-induced strain field,  $\varepsilon(t)$ , set by the ‘‘phonon-tunneling system coupling coefficient’’ or ‘‘deformation potential’’,  $\gamma = (1/2)\partial\Delta/\partial\varepsilon$  [S16]. In general, these two quantities would be tensors, describing the anisotropic nature of the crystal, however, we have simplified this analysis by considering a particular strain symmetry so that we can treat their inner product as an effective strain,  $\varepsilon(t)$ , multiplied by a deformation potential,  $\gamma$ , both of which are scalars [S16]. Furthermore, we note that we have neglected to include the off-diagonal elements in Eq. (S11), due to the fact that strain variations in the solid have a much larger effect on the asymmetry energy than they do on the tunnel splitting [S15, S16, S18]. Perturbing the asymmetry energy in this way acts to shift the energy separation between the TLS states to

$$E'(t) = E + \delta E(t), \quad (\text{S13})$$

where to first order  $\delta E(t) = 2\gamma\Delta\varepsilon(t)/E$ . This shift in the separation energy will additionally perturb the population of the excited state of the TLS away from equilibrium, leading to a time-dependent occupation probability

$$p_+(t) = p_+^0 + \delta p_+(t), \quad (\text{S14})$$

where  $\delta p_+(t)$  is the instantaneous deviation of the excitation probability away from its equilibrium value in the absence of the phonon-induced strain given by Eq. (S9). Note that while we choose to focus on the excitation probability, a similar shift will occur for the ground state probability,  $p_-(t)$ , which will be related to  $p_+(t)$  via the conservation of probability,  $p_-(t) + p_+(t) = 1$ .

In order to determine  $\delta p_+(t)$ , we must first realize that the perturbed system will strive towards a new, time-dependent equilibrium excitation probability,  $\bar{p}_+(t)$ , which can be found by inputting

Eq. (S13) into the expression for  $p_+^0$  in Eq. (S9) and expanding to first order to obtain

$$\bar{p}_+(t) = \frac{1}{e^{E'(t)/k_B T} + 1} \approx p_+^0 + \frac{dp_+^0}{dE} \frac{2\gamma\Delta}{E} \varepsilon(t) = p_+^0 - \frac{\gamma\Delta}{2k_B T E} \text{sech}^2\left(\frac{E}{2k_B T}\right) \varepsilon(t). \quad (\text{S15})$$

This ‘‘instantaneous’’ equilibrium probability can be interpreted as the excitation probability that the system would reach if the TLS energy separation stayed at  $E'(t)$  for a sufficiently long time. However, the TLS cannot immediately achieve this new equilibrium, as it must do so by exchanging energy with the surrounding phonon bath, evolving according to [S15]

$$\dot{p}_+ = -p_+\nu_{+-} + p_-\nu_{-+}, \quad (\text{S16})$$

where  $\nu_{+-}$  ( $\nu_{-+}$ ) is the phonon-induced transition rate from the excited (ground) state to the ground (excited) state. By looking at the steady state of Eqs. (S15) and (S16), we can see that these transition rates obey the condition of detailed balance, such that  $\nu_{-+}/\nu_{+-} = p_+^0/p_-^0 = \bar{p}_+(t)/\bar{p}_-(t) = e^{-E/k_B T}$  [S10, S16]. Using this relation, along with the conservation of probability, Eq. (S16) can be rewritten as

$$\dot{p}_+ = -p_+(\nu_{+-} + \nu_{-+}) + \nu_{-+} = -p_+\tau^{-1} + \nu_{-+} = -\frac{p_+ - \bar{p}_+}{\tau}, \quad (\text{S17})$$

where we have introduced the relaxation rate of the excited state

$$\tau^{-1} = \nu_{+-} + \nu_{-+} = \nu_{+-}(1 + e^{-E/k_B T}). \quad (\text{S18})$$

This rate can be interpreted as the inverse of the relaxation time,  $\tau$ , required for the excitation probability to relax back to its steady-state value after it has been perturbed from equilibrium. By inputting Eq. (S15) into Eq. (S17), while using the fact that  $\dot{p}_+(t) = \dot{\delta p}_+(t)$ , we find

$$\tau \dot{\delta p}_+ = -\delta p_+ - \frac{\gamma\Delta}{2k_B T E} \text{sech}^2\left(\frac{E}{2k_B T}\right) \varepsilon(t). \quad (\text{S19})$$

This equation can be solved by Fourier transforming to obtain

$$\delta p_+(\omega) = -\frac{\gamma\Delta}{2k_B T E} \text{sech}^2\left(\frac{E}{2k_B T}\right) \frac{\varepsilon(\omega)}{1 - i\omega\tau}, \quad (\text{S20})$$

resulting in a frequency domain solution for the deviation of the excitation probability from equilibrium.

We now look to find an expression for the TLS relaxation rate given in Eq. (S18). This can be done by applying a Fermi's Golden Rule calculation to the perturbation Hamiltonian in Eq. (S12), to determine the transition rate from the excited state to the ground state as [S15, S18]

$$\nu_{+-} = \sum_j \sum_{n_j} \frac{2\pi}{\hbar} |\langle \psi_f | H'_j | \psi_i \rangle|^2 g_j(\hbar\omega) \delta(E - \hbar\omega). \quad (\text{S21})$$

The first sum is performed over the polarizations of the phonon radiation modes, labelled by the subscript  $j$  (one longitudinal, two transverse), each with a 3D Debye density of states  $g_j(\hbar\omega) = \omega^2/2\pi^2\hbar c_j^3$  [S15] and a speed of sound  $c_j$ . The second sum is to ensure that all possible phononic states of the solid are considered, where  $\psi_i = |\psi_+, n_j\rangle$  is the initial state of the composite TLS-phonon system, with the TLS in its excited state and  $n_j$  phonons in the  $j$ th polarization mode, whereas in the final state,  $\psi_f = |\psi_-, n_j + 1\rangle$ , the TLS has de-excited, creating an additional phonon in the process [S16]. The delta function,  $\delta(E - \hbar\omega)$ , constrains the emitted phonon of frequency  $\omega$  to match the energy separation of the TLS. Finally,  $H_j$  is the perturbation Hamiltonian for each phonon polarization, obtained by replacing  $\varepsilon(t)$  in Eq. (S12) with the strain,  $\varepsilon_j(t)$ , corresponding to the  $j$ th mode with wavenumber  $k_j$ . We can express these strains in terms of the annihilation,  $b_{k_j}$ , and creation,  $b_{-k_j}^\dagger$ , operators for each of these phononic polarization modes as [S15, S19]

$$\varepsilon_j(t) = k_j \sqrt{\frac{\hbar}{2\rho\omega}} \left( b_{k_j} e^{-i\omega t} + b_{-k_j}^\dagger e^{i\omega t} \right), \quad (\text{S22})$$

where  $\rho$  is the mass density of the solid. Using this operator, we determine the transition rate of the excited state as

$$\nu_{+-} = A\Delta_0^2 E (\langle n_j \rangle + 1), \quad (\text{S23})$$

where  $\langle n_j \rangle = (e^{E/k_B T} - 1)^{-1}$  is the average phonon occupation of the  $j$ th polarization mode according to Bose-Einstein statistics. Inputting this expression into Eq. (S18), we find

$$\tau^{-1} = A\Delta_0^2 E \coth\left(\frac{E}{2k_B T}\right), \quad (\text{S24})$$

where

$$A = \sum_j \frac{\gamma_j^2}{2\pi\rho c_j^5 \hbar^4} = \left( \frac{\gamma_l^2}{c_l^5} + 2 \frac{\gamma_t^2}{c_t^5} \right) \frac{1}{2\pi\rho \hbar^4}, \quad (\text{S25})$$

with  $\gamma_j$  being the deformation potential associated with the  $j = l, t$  polarizations, corresponding to the longitudinal and transverse modes, respectively.

To analyze how the delay in equilibration due this finite relaxation rate affects the propagation of acoustic waves in the material, we start by determining the perturbed internal energy of the system due to the TLS defects, which can be found by inputting Eq. (S13) into Eq. (S10) to obtain

$$U'(t) = N \left( E + \frac{2\gamma\Delta}{E} \varepsilon(t) \right) \left( p_+(t) - \frac{1}{2} \right). \quad (\text{S26})$$

From this internal energy, we can determine the TLS-induced stress in the solid as [S10, S20]

$$\sigma'(t) = \frac{1}{V} \frac{\partial U'}{\partial \varepsilon} \Big|_{p_+} = D_0 \left( p_+(t) - \frac{1}{2} \right) \frac{2\gamma\Delta}{E} = \sigma + \delta\sigma(t), \quad (\text{S27})$$

where we have held the excitation probability constant and divided by the volume of the solid,  $V$ , such that  $D_0 = N/V$  is the average spatial density of the TLS defects. The deviation,  $\delta\sigma(t)$ , from the static component of the TLS-induced stress,  $\sigma$ , is then found by inputting Eq. (S14) for  $p_+(t)$  into Eq. (S27), resulting in

$$\delta\sigma(t) = \frac{2\gamma\Delta D_0}{E} \delta p_+(t). \quad (\text{S28})$$

Fourier transforming Eq. (S28) and using Eq. (S20) for  $\delta p_+(\omega)$ , we obtain

$$\delta\sigma(\omega) = - \left( \frac{\Delta}{E} \right)^2 \frac{D_0 \gamma^2}{k_B T} \text{sech}^2 \left( \frac{E}{2k_B T} \right) \frac{\varepsilon(\omega)}{1 - i\omega\tau}, \quad (\text{S29})$$

explicitly quantifying the phase lag between the stress and strain in the material due to phonon-TLS coupling. To determine how exactly this delay leads to acoustic attenuation, we turn to the perturbed elastic modulus of the material,  $K'(\omega) = K + \delta K(\omega) \equiv \sigma'(\omega)/\varepsilon(\omega)$ , where  $K$  is the static portion of the elastic modulus and the dynamic component is given by [S10]

$$\delta K(\omega) = \frac{\delta\sigma(\omega)}{\varepsilon(\omega)} = - \left( \frac{\Delta}{E} \right)^2 \frac{D_0 \gamma^2}{k_B T} \text{sech}^2 \left( \frac{E}{2k_B T} \right) \frac{1}{1 - i\omega\tau}. \quad (\text{S30})$$

The acoustic attenuation coefficient, defined as the inverse of the phonon mean free path  $l$ , is then

found to be [S10]

$$\alpha(\omega) \equiv l^{-1} = 2\text{Im}\{k\} = 2\text{Im}\left\{\frac{\omega}{c'(\omega)}\right\} = -\frac{\omega}{\rho c^3}\text{Im}\{\delta K(\omega)\}, \quad (\text{S31})$$

where we have used the expression  $c'(\omega) = \sqrt{K'(\omega)/\rho}$  for the frequency-dependent speed of sound in the material, such that the speed of sound in the absence of TLS is given by  $c = \sqrt{K/\rho}$  [S21]. Note that the factor of two arises from the fact that  $\alpha(\omega)$  describes the decay of the acoustic intensity, not its amplitude [S18]. Inputting Eq. (S30) for  $\delta K(\omega)$  into Eq. (S31), we find an explicit expression for the attenuation coefficient as

$$\alpha(\omega) = \left(\frac{\Delta}{E}\right)^2 \frac{D_0\gamma^2}{\rho c^3 k_B T} \text{sech}^2\left(\frac{E}{2k_B T}\right) \frac{\omega^2\tau}{1 + \omega^2\tau^2}. \quad (\text{S32})$$

Finally, the dissipation of a mechanical mode at frequency,  $\omega_m$ , due to coupling with TLS defects, defined as its inverse quality factor, is given by

$$Q_{\text{TLS}}^{-1} = \frac{\alpha(\omega_m)c}{\omega_m} = \left(\frac{\Delta}{E}\right)^2 \frac{D_0\gamma^2}{\rho c^2 k_B T} \text{sech}^2\left(\frac{E}{2k_B T}\right) \frac{\omega_m\tau}{1 + \omega_m^2\tau^2}, \quad (\text{S33})$$

from which we can find the mechanical damping rate due to TLS as

$$\Gamma_{\text{TLS}} = \omega_m Q_{\text{TLS}}^{-1} = \left(\frac{\Delta}{E}\right)^2 \frac{D_0\gamma^2}{\rho c^2 k_B T} \text{sech}^2\left(\frac{E}{2k_B T}\right) \frac{\omega_m^2\tau}{1 + \omega_m^2\tau^2}. \quad (\text{S34})$$

### C. Coupling to Ensembles of TLS Defects with Varying Energy Distributions

Up to this point, we have considered coupling of the mechanical mode to a collection of  $N$  TLS defects within the volume  $V$  of the solid, all of which have identical asymmetry energy,  $\Delta$ , and tunnel splitting,  $\Delta_0$ . However, in a realistic material, variations in the TLS environment due to disorder will lead to a distribution in  $\Delta$  and  $\Delta_0$ . These effects can be accounted for by replacing the TLS density,  $D_0$ , by an integral over a distribution function,  $h(\Delta, \Delta_0)$ , defined such that [S22]

$$D_0 = \int_0^\infty \int_0^\infty h(\Delta, \Delta_0) d\Delta d\Delta_0. \quad (\text{S35})$$

Making this modification to Eq. (S34), we find the damping rate of the mechanical resonator due to relaxation coupling to a TLS ensemble as

$$\Gamma_{\text{TLS}} = \frac{\gamma^2}{\rho c^2 k_B T} \int_0^\infty \int_0^\infty \left(\frac{\Delta}{E}\right)^2 \text{sech}^2\left(\frac{E}{2k_B T}\right) \frac{\omega_m^2 \tau}{1 + \omega_m^2 \tau^2} h(\Delta, \Delta_0) d\Delta d\Delta_0. \quad (\text{S36})$$

The functional form of  $h(\Delta, \Delta_0)$  is chosen to characterize the energy distribution of the TLS ensemble and has a drastic effect on the temperature dependence of the material's damping rate. For instance, in amorphous solids, a distribution function of  $h(\Delta, \Delta_0) \propto 1/\Delta_0$  is chosen, as it reflects the broad distribution of  $\Delta$  and  $\Delta_0$  exhibited due to the lack of long range order in these glassy materials, resulting in a low temperature damping rate that varies as  $T^3$  [S15, S16]. However, such a distribution function poorly describes the situation of a crystalline solid, whereby an ordered lattice results in a narrow distribution of TLS energies. To account for this, Phillips [S14] suggested a distribution function of the form

$$h(\Delta, \Delta_0) = D_0 \sqrt{\frac{2}{\pi}} \frac{1}{\delta \Delta} e^{-\frac{1}{2} \left(\frac{\Delta}{\delta \Delta}\right)^2} \delta(\Delta_0 - \bar{\Delta}_0), \quad (\text{S37})$$

that is to say that the crystalline nature of the solid results in a well-defined tunneling energy of  $\bar{\Delta}_0$  and a gaussian spread in the asymmetry energy, centered around  $\Delta = 0$  with a standard deviation of  $\delta \Delta$ . With this choice of distribution function, we need only consider the relevant case of  $\omega_m \tau > 1$ , due to the fact that the experimentally measured dissipation increases monotonically with temperature for each mode studied in the main text [S14]. This allows us to approximate the mechanical damping rate in Eq. (S36) as

$$\Gamma_{\text{TLS}} = \frac{\gamma^2}{\rho c^2 k_B T} \int_0^\infty \int_0^\infty \left(\frac{\Delta}{E}\right)^2 \text{sech}^2\left(\frac{E}{2k_B T}\right) \tau^{-1}(\Delta, \Delta_0) h(\Delta, \Delta_0) d\Delta d\Delta_0, \quad (\text{S38})$$

where we have now expressed  $\tau$  as an explicit function of  $\Delta$  and  $\Delta_0$ .

In this form, we can examine the high temperature limit of the mechanical damping rate. Taking  $T \gg (\delta \Delta^2 + \bar{\Delta}_0^2)^{1/2}/k_B$ , we can make the approximations  $\text{sech}^2(E/2k_B T) \approx 1$  and  $\coth(E/2k_B T) \approx 2k_B T/E$ , such that  $\tau^{-1}(\Delta, \Delta_0) \approx 2A\Delta_0^2 k_B T$  for the regions of integration in Eq. (S38) that provide the majority of the contribution to  $\Gamma_{\text{TLS}}$ . Therefore, we can express the high

temperature damping rate as

$$\tilde{\Gamma}_{\text{TLS}} \approx \frac{2C\bar{\Delta}_0^2}{\delta\Delta} \sqrt{\frac{2}{\pi}} \int_0^\infty \left(\frac{\Delta}{\bar{E}}\right)^2 e^{-\frac{1}{2}\left(\frac{\Delta}{\delta\Delta}\right)^2} d\Delta, \quad (\text{S39})$$

where  $C = A\gamma^2 D_0/\rho c^2$  and  $\bar{E}^2 = \Delta^2 + \bar{\Delta}_0^2$ . Note that the factor of  $k_B T$  in  $\tau^{-1}$  cancels that in the denominator of Eq. (S38), such that  $\tilde{\Gamma}_{\text{TLS}}$  is temperature independent.

We conclude this section with a final comment that due to the varying orientation of the mechanical motion with respect to the symmetry axes of the crystal, each mode will have a unique  $\gamma$  and  $c$ , however, determining exact values for these parameters is beyond the scope of this work.

## S5. STRAIN ENERGY AND EFFECTIVE VOLUME

As discussed in the previous section, it is the strain induced by the motion of the mechanical resonator that couples to the TLS defects in the device's material. It is therefore important to understand the spatially-varying strain profiles of each mechanical mode. To do this, we look at the strain energy density of each mode, time-averaged over the mechanical period of oscillation,  $\tau_0$ , to give [S23, S24]

$$W(\vec{r}) = \frac{1}{\tau_0} \int_0^{\tau_0} \frac{1}{2} \sum_{i,j,k,l} K_{ijkl} \varepsilon_{ij}(\vec{r}, t) \varepsilon_{kl}(\vec{r}, t) dt. \quad (\text{S40})$$

Here,  $K_{ijkl}$  is the elasticity tensor of the material (*i.e.* the tensorial version of the elastic modulus  $K$  in the previous section) and  $\varepsilon_{ij}(\vec{r}, t)$  are the strains in the solid, defined as

$$\varepsilon_{ij}(\vec{r}, t) = \frac{1}{2} \left( \frac{\partial u_i(\vec{r}, t)}{\partial x_j} + \frac{\partial u_j(\vec{r}, t)}{\partial x_i} \right), \quad (\text{S41})$$

where  $u_i(\vec{r}, t)$  and  $x_i$  are the  $i$ th components of the displacement and coordinate vectors, respectively.

For systems that exhibit cubic symmetry, such as the diamond lattice of silicon, the elasticity tensor has only three independent, nonzero components, namely  $K_{xxxx} = K_{yyyy} = K_{zzzz} = K_{11} = 165.6$  GPa,  $K_{xxyy} = K_{xxzz} = K_{yyzz} = K_{yyxx} = K_{zzxx} = K_{zzyy} = K_{12} = 63.9$  GPa and  $K_{xyxy} = K_{xzzz} = K_{yzyz} = K_{44} = 79.5$  GPa, with all other components being zero [S21]. This

simplifies the energy density of Eq. (S40) to

$$W(\vec{r}) = \frac{1}{\tau_0} \int_0^{\tau_0} \frac{1}{2} \left[ K_{11} (\varepsilon_{xx}^2(\vec{r}) + \varepsilon_{yy}^2(\vec{r}) + \varepsilon_{zz}^2(\vec{r})) + 4K_{44} (\varepsilon_{xy}^2(\vec{r}) + \varepsilon_{xz}^2(\vec{r}) + \varepsilon_{yz}^2(\vec{r})) + 2K_{12} (\varepsilon_{xx}(\vec{r})\varepsilon_{yy}(\vec{r}) + \varepsilon_{xx}(\vec{r})\varepsilon_{zz}(\vec{r}) + \varepsilon_{yy}(\vec{r})\varepsilon_{zz}(\vec{r})) \right] dt. \quad (\text{S42})$$

The total (time-averaged) stored elastic energy will then simply be given by

$$E_s = \int W(\vec{r}) dV, \quad (\text{S43})$$

where the integral is performed over the entire volume of the solid in question.

As can be seen in Fig. 4 of the main text, the majority of the strain energy density is localized to certain portions of the resonator, such that the mechanical motion will only couple to a specific subset of TLS defects that occupy the regions of high strain. To characterize the extent to which the mechanical motion of the resonator probes the TLS, we have defined an effective strain volume

$$V_{\text{str}} = \int \frac{W(\vec{r})}{\max[W(\vec{r})]} dV, \quad (\text{S44})$$

analogous to the effective mode volumes for optical cavities in cavity quantum electrodynamics (see Section S2), where  $\max[W(\vec{r})]$  is the maximum value of the strain energy density. Note that with this choice of effective volume, the stored elastic energy then becomes  $E_s = \max[W(\vec{r})]V_{\text{str}}$ . The effective strain volumes are calculated using FEM simulations of the strain energy density profiles for each of the four mechanical modes considered in this work (see Fig. 4 and Table I in the main text for the simulated strain energy density profiles and corresponding values of  $V_{\text{str}}$ ).

## S6. ESTIMATION OF TWO-LEVEL SYSTEM DENSITIES

Here we describe the method we use to provide an estimate for the spatial density,  $D_0$ , as well as the corresponding number of defects,  $N$ , for the TLS ensemble coupled to each of the four mechanical modes studied in this work. This is done by rearranging the expression for the fit parameter  $C$  (see Eq. (S39)) to solve for the TLS density as

$$D_0 = \frac{\rho c^2 C}{A \gamma^2}. \quad (\text{S45})$$

In general, due to the crystalline nature of the silicon, the values of  $\gamma$  and  $c$ , and therefore  $A$ , will vary depending on the mechanical mode considered. However, as an approximation, we assume these parameters to be mode-independent, *i.e.*  $\gamma_j \approx \gamma$  and  $c_j \approx c$  for each of the  $j$  phonon polarizations, such that  $A \approx 3\gamma^2/2\pi\rho c^5\hbar^4$  (see Eq. (S25)) and

$$D_0 \approx \frac{2\pi\rho^2 c^7 \hbar^4 C}{3\gamma^4}. \quad (\text{S46})$$

Finally, only TLS defects that are located within the effective strain volume,  $V_{\text{str}}$ , of each mechanical mode will contribute to its damping, such that the number of active TLS defects is given by  $N = D_0 V_{\text{str}}$ . Numerical values for  $N$  and  $D_0$  for each mechanical mode, calculated using  $C$  as determined from the fits to the experimental data in Fig. 4 of the main text, along with the material properties for boron-doped silicon found in the literature ( $\rho = 2330 \text{ kg/m}^3$  [S17],  $c = 5870 \text{ m/s}$  [S25] and  $\gamma = 3 \text{ eV}$  [S25, S26]), can be seen in Table I of the main text.

## S7. MECHANICAL RESONATOR HEATING MODEL

We model the thermalization of a given mode of our mechanical resonator as a harmonic oscillator at frequency,  $\omega_m$ , coupled at its intrinsic damping rate,  $\Gamma_i$ , to a cold environmental bath at temperature,  $T$ , as well as at a rate,  $\Gamma_p$ , to a hot phonon bath at temperature,  $T_p$ , due to optical absorption of measurement photons, as depicted in Fig. S3a. Due to the high quality factors of the mechanical modes considered, we can also treat these baths as harmonic oscillators at the mechanical frequency, such that their average thermal occupancy will be Bose-Einstein distributed according to  $n_\delta = (e^{\hbar\omega_m/k_B T_\delta} - 1)^{-1}$ , where  $T_\delta$  is the temperature of the corresponding bath. In this situation, the rate equation for the average occupation of the mechanical mode will be given by [S27]

$$\langle \dot{n} \rangle = -\Gamma \langle n \rangle + \Gamma_i n_{\text{th}} + \Gamma_p n_p, \quad (\text{S47})$$

with  $\Gamma = \Gamma_i + \Gamma_p$  being the total rate at which the mode equilibrates to the two baths. Solving this rate equation, we find the time-dependent mechanical mode occupancy to be

$$\langle n \rangle (t) = \langle n \rangle (t_0) e^{-\Gamma(t-t_0)} + n_{\text{eq}} (1 - e^{-\Gamma(t-t_0)}), \quad (\text{S48})$$

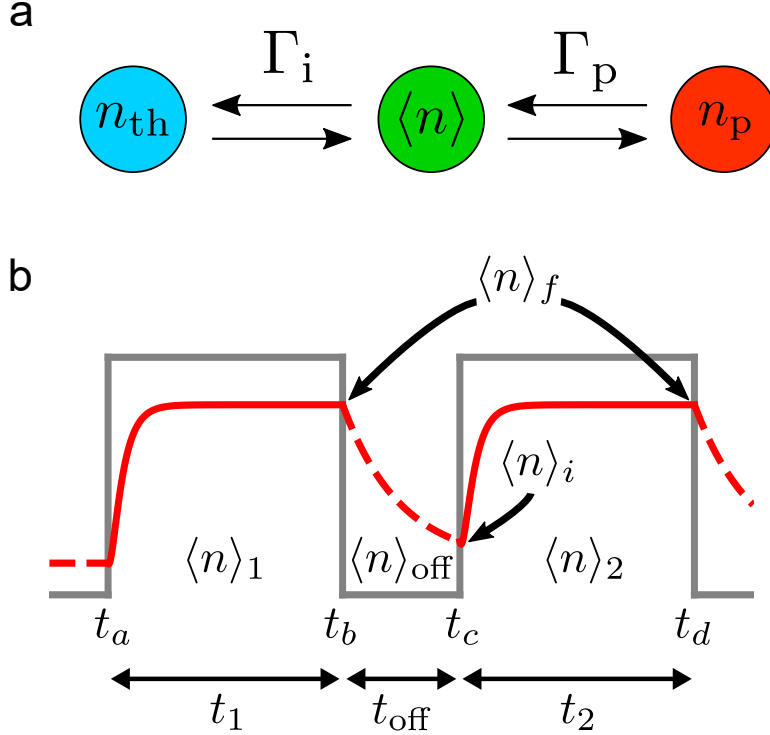


FIG. S3. **Mechanical heating model and double pulsing schematic.** **a**, Block diagram of the heating model for the experimentally relevant case where the mechanical mode is coupled to a cold environmental bath at its intrinsic damping rate,  $\Gamma_i$ , and a hot photon-induced bath at a rate,  $\Gamma_p$ , each with phonon occupancies of  $n_{\text{th}}$  and  $n_p$ , respectively. **b**, Diagram of the double pulse measurement scheme used in the main text. The solid grey line indicates the duty cycle of the laser, while the solid (dashed) red line expresses the phonon occupation of the mechanical mode with the laser on (off).

where  $\langle n \rangle(t_0)$  is the phonon occupancy at the initial time  $t_0$  and  $n_{\text{eq}} = (\Gamma_i n_{\text{th}} + \Gamma_p n_p) / \Gamma$  is the final occupancy of the mechanical mode at times  $t \gg \Gamma^{-1}$ , long enough such that the mode is able to equilibrate to an average of the bath occupations, weighted by their coupling rates. Furthermore, if the connection to the hot photon-induced bath is severed (*i.e.* by turning the laser off), we take  $n_p = 0$ ,  $T_p = 0$  such that the mechanical mode occupation will tend towards equilibrium with the environmental bath at its intrinsic damping rate according to

$$\langle n \rangle(t) = \langle n \rangle(t_0) e^{-\Gamma_i(t-t_0)} + n_{\text{th}} (1 - e^{-\Gamma_i(t-t_0)}). \quad (\text{S49})$$

For the experiment considered in this paper, we measure the low temperature damping rate of our mechanical device, using the pump/probe measurement outlined in Section S1 A. This procedure can be described by the general two pulse scheme depicted in Fig. S3b, where a pump pulse, which turns on at  $t = t_a$  and off at  $t = t_b$  (pulse length  $t_1 = t_b - t_a$ ), is followed by a probe pulse

that turns on at  $t = t_c$  and off at  $t = t_d$  (pulse length  $t_2 = t_d - t_c$ ), with a delay between the two pulses of  $t_{\text{off}} = t_c - t_b$ . For this situation, the occupation of the mechanical mode during the pump pulse will evolve in time according to Eq. (S48) as

$$\langle n \rangle_1(t) = \langle n \rangle(t_a) e^{-\Gamma(t-t_a)} + n_{\text{eq}} (1 - e^{-\Gamma(t-t_a)}). \quad (\text{S50})$$

Once the pump pulse has been turned off, the resonator's occupancy will cool towards that of the environmental bath, as governed by Eq. (S49) to give

$$\langle n \rangle_{\text{off}}(t) = \langle n \rangle(t_b) e^{-\Gamma_i(t-t_b)} + n_{\text{th}} (1 - e^{-\Gamma_i(t-t_b)}). \quad (\text{S51})$$

Finally, the occupation of the mechanical mode during the probe pulse will obey

$$\langle n \rangle_2(t) = \langle n \rangle(t_c) e^{-\Gamma(t-t_c)} + n_{\text{eq}} (1 - e^{-\Gamma(t-t_c)}). \quad (\text{S52})$$

Assuming the experimentally relevant case of  $t_1 = t_2 \gg \Gamma^{-1}$ , the final occupancy at the end of either the pump or probe pulse will be given by  $\langle n \rangle(t_b) = \langle n \rangle(t_d) = n_{\text{eq}}$ , while the initial occupancy of the mode at the beginning of the probe pulse can be found to be  $\langle n \rangle(t_c) = n_{\text{eq}} e^{-\Gamma_i t_{\text{off}}} + n_{\text{th}} (1 - e^{-\Gamma_i t_{\text{off}}})$ . Using these two expressions, we can determine the ratio of the *measured* occupancy at the beginning of the probe pulse,  $\langle n \rangle_i$ , to the final *measured* occupancy of either the probe or the pump pulse as

$$\frac{\langle n \rangle_i}{\langle n \rangle_f} = \frac{\langle n \rangle(t_c) + n_{\text{imp}}}{\langle n \rangle(t_b) + n_{\text{imp}}} = \frac{\langle n \rangle(t_c) + n_{\text{imp}}}{\langle n \rangle(t_d) + n_{\text{imp}}} = \frac{(n_{\text{eq}} - n_{\text{th}}) e^{-\Gamma_i t_{\text{off}}} + n_{\text{th}} + n_{\text{imp}}}{n_{\text{eq}} + n_{\text{imp}}}, \quad (\text{S53})$$

where we have included the noise due to the imprecision of the measurement as an apparent phonon occupancy  $n_{\text{imp}}$ . Using this equation, thermal ringdown data for the mechanical mode can be fit to extract its intrinsic damping rate, as is done in the main text.

We conclude on the note that it is often the case that  $n_{\text{eq}} \approx n_p \gg n_{\text{th}}, n_{\text{imp}}$ , such that Eq. (S53) simplifies to

$$\frac{\langle n \rangle_i}{\langle n \rangle_f} \approx e^{-\Gamma_i t_{\text{off}}} + \frac{n_{\text{th}} + n_{\text{imp}}}{n_{\text{eq}}}, \quad (\text{S54})$$

as can be seen by the fact that  $\langle n \rangle_i / \langle n \rangle_f \approx 1$  for  $t_{\text{off}} \ll \Gamma_i^{-1}$  in Fig. 3b of the main text.

- 
- [S1] Eichenfield, M., Chan, J., Safavi-Naeini, A. H., Vahala, K. J. & Painter, O. Modeling dispersive coupling and losses of localized optical and mechanical modes in optomechanical crystals. *Opt. Express* **17**, 20078-20098 (2009).
- [S2] Hauer, B. D., Doolin, C., Beach, K. S. D. & Davis, J. P. A general procedure for thermomechanical calibration of nano/micro-mechanical resonators. *Ann. Phys.* **339**, 181-207 (2013).
- [S3] Vahala, K. J. *Optical Microcavities - Advanced Series in Applied Physics: Vol. 5* (World Scientific, Singapore, 2004).
- [S4] Johnson, S. G. *et al.* Perturbation theory for Maxwell's equations with shifting material boundaries. *Phys. Rev. E* **65**, 066611 (2002).
- [S5] Hauer, B. D., Maciejko, J. & Davis, J. P. Nonlinear power spectral densities for the harmonic oscillator. *Ann. Phys.* **361**, 148-183 (2015).
- [S6] Zeller, R. C. & Pohl, R. O. Thermal conductivity and specific heat of noncrystalline solids. *Phys. Rev. B* **4**, 2029-2041 (1971).
- [S7] Anderson, P. W., Halperin, B. I. & Varma, C. M. Anomalous low-temperature thermal properties of glasses and spin glasses. *Philos. Mag.* **25**, 1-9 (1972).
- [S8] Phillips, W. A. Tunneling states in amorphous solids. *JLTP* **7**, 351-360 (1972).
- [S9] Jäckle, J. On the ultrasonic attenuation in glasses at low temperatures. *Z. Physik* **257**, 212-223 (1972).
- [S10] Jäckle, J., Piché, L., Arnold, W. & Hunklinger, S. Elastic effects of structural relaxation in glasses at low temperatures. *J. Non-Crys. Solids* **20**, 365-391 (1976).
- [S11] Heinicke, W., Winterling, G. & Dransfeld, K. Low-temperature measurement of the hypersonic absorption in fused quartz by stimulated Brillouin scattering. *J. Acoust. Soc. Am.* **49**, 954-958 (1971).
- [S12] Kleiman, R. N., Agnolet, G. & Bishop, D. J. Two-level systems observed in the mechanical properties of single-crystal silicon at low temperatures. *Phys. Rev. Lett.* **59**, (1987).
- [S13] Mihailovich, R. E. & Parpia, J. M. Anomalous low temperature mechanical properties of single-crystal silicon. *Physica B* **165/166**, 125-126 (1990).
- [S14] Phillips, W. A. *Phys. Rev. Lett.* **61**, 2632 (1988).
- [S15] Phillips, W. A. Two-level states in glasses. *Rep. Prog. Phys.* **50**, 1657-1708 (1987).
- [S16] Esquinazi, P. *Tunneling Systems in Amorphous and Crystalline Solids* (Springer-Verlag, Berlin, 1998).

- [S17] Zolfagharkhani, G., Gaidarzhy, A., Shim, S.-B., Badzey, R. L. & Mohanty, P. Quantum friction in nanomechanical oscillators at millikelvin temperatures. *Phys. Rev. B* **72**, 224101 (2005).
- [S18] Enss, C. & Hunklinger, S. *Low-Temperature Physics* (Springer-Verlag, Berlin, 2005)
- [S19] Kittel, C. *Quantum Theory of Solids* (Wiley, New York, 1963).
- [S20] Landau, L. D., Pitaevskii, L. P., Kosevich, A. M. & Lifshitz, E. M. *Theory of Elasticity, Third Edition: Vol. 7* (Butterworth-Heinemann, London, 1986).
- [S21] Mason, W. P. *Physical Acoustics and the Properties of Solids* (Nostrand, Princeton, 1958).
- [S22] Hunklinger, S. & Arnold, W. *Chapter 3 - Ultrasonic Properties of Glass at Low Temperature - Physical Acoustics, Vol. XII* ed. Mason, W. P. & Thurston, R. N. (Academic, New York, 1976).
- [S23] Achenbach, J. D., *Wave Propagation in Elastic Solids* (North-Holland, Amsterdam, 1973).
- [S24] Sadd, M. H., *Elasticity: Theory, Applications, and Numerics* (Academic Press, Burlington, 2005).
- [S25] Fjeldy, T., Ishiguro, T. & Elbaum, C. Heat-pulse propagation in *p*-type Si and Ge under uniaxial stress. *Phys. Rev. B* **7**, 1392-1410 (1973).
- [S26] Mihailovich, R. E. & Parpia, J. M. Low temperature mechanical properties of boron-doped silicon. *Phys. Rev. Lett.* **68**, 3052-3055 (1992).
- [S27] Meenehan, S. M. *et al.* Pulsed excitation dynamics of an optomechanical crystal resonator near its quantum ground state of motion. *Phys. Rev. X* **5**, 041002 (2015).